IEEE Open Journal of the
Communications Society

Received XX Month, XXXX; revised XX Month, XXXX; accepted XX Month, XXXX; Date of publication XX Month, XXXX; date of current version XX Month, XXXX.

Multi-Laser Powered UAV Swarm for Extended Offshore Coverage

Amr M. Abdelhady, ***Senior Member, IEEE,*** **Osama Amin,** ***Senior Member, IEEE*****,**
Basem Shihada, ***Senior Member, IEEE*****, George Turkiyyah**

[1] Computer Electrical, and Mathematical Science and Engineering (CEMSE) Division, King Abdullah University of Science and Technology (KAUST), Thuwal, Makkah Province, Kingdom of Saudi Arabia

---

ABSTRACT In this work, we propose employing multi-laser powered unmanned aerial vehicle (UAV) swarms to provide wireless communications coverage for distant offshore users. Towards this end, we formulate the total spectral efficiency and worst-case spectral efficiency maximization problems while considering UAVs' 3D locations, lasers power allocation, and UAVs' radiated power as the system degrees of freedom. We solve these problems using the single-block successive convex approximation (SCA) approach, for which we derive a novel SCA-compatible bound for the harvested power. Finally, we assess the efficacy of the proposed solutions via numerical simulations, sweeping over different system parameters as the number of laser sources, UAVs, the maximum laser output power, and the laser sources locations. The numerical results show that our proposed solution provides 15-40% optimization gains over the considered low-complexity benchmark. In addition, total and worst-case spectral efficiency performance gains, up to 33% and 60%, respectively, are observed compared with tethered swarm architecture under low atmospheric turbulence assumptions. Moreover, numerical results reveal that there is an optimal number of swarm UAVs that is coupled with the available system energy budget.

INDEX TERMS Maritime communications, laser-powered UAVs, multi-laser, UAV swarm optimization, resource allocation, offshore coverage, single-block successive convex approximation (SCA), wireless networks.

I. Introduction

OVER recent decades, the interest in maritime activities such as ocean exploration, shipping, cruises, fishing, and environmental monitoring has witnessed a significant rise. Seaborne trade volume, a key indicator, grew by 21.5% since 2010 to reach 11.08 billion tons in 2019, and the global container fleet expanded by over 32% in the same decade, according to the United Nations Conference on Trade and Development (2019) [1]. Accordingly, the need for different types of communications coverage over seas and oceans has surged and highlighted the critical challenges of maritime connectivity [2]–[5]. According to the Global Maritime Trends 2050 report [6], 11-17% of the global shipping fleet is projected to be autonomous by 2040, transforming the global maritime industry and necessitating robust, reliable, and high-capacity communication networks to support remote operations, real-time monitoring, and data exchange. Currently, research efforts are focusing on addressing these challenges through various approaches, extended from purely terrestrial solutions to integrated non-terrestrial networks and specialized unmanned aerial vehicle (UAV) systems.

Initial research efforts focused on terrestrially supported maritime communication network solutions to provide service to offshore areas [7]–[10]. These approaches primarily employed advanced beamforming techniques with various optimization objectives: maximizing minimum data rates via multi-timescale beamforming [7], minimizing power consumption through cooperative terrestrial-maritime schemes [8], [9], and ensuring robust communications under imperfect channel conditions caused by sea wave fluctuations [10]. Notably, studies like [9] explored enhancing performance by equipping maritime relays with both active relays and passive Reconfigurable Intelligent Surface (RIS) setups. Despite these advancements, purely terrestrial solutions face fundamental limitations in providing coverage to distant offshore areas due to base station location constraints, signal propagation challenges, and the curvature of the Earth.

To overcome the limitations of terrestrial-only networks, integrated terrestrial and non-terrestrial maritime networks have emerged as a promising approach for comprehensive maritime coverage [2], [11], [12]. Maritime environments present unique challenges, including heterogeneous communication demands, sparse user spatial density, and inherently dynamic wireless channels. Heterogeneous demands stem from diverse user types with varying throughput and reliability requirements, complicating resource allocation. Sparse spatial density renders fixed infrastructure economically impractical, necessitating flexible and adaptive network architectures capable of dynamically adjusting deployment configurations and resource management to the spatially and temporally varying demand patterns encountered in maritime environments. Such characteristics make the maritime network architecture design, deployment configuration and resources management critical. Subsequently, research in this domain has explored various approaches: stochastic geometry modeling for satellite-based communications [13], synergistic deployment of terrestrial base stations with LEO satellites [14], and hybrid architectures combining satellites with tethered UAVs [15], [16]. In particular, in [13] the authors assess the system-level, coverage probability, performance of satellite-based maritime networking while capturing the sparse spatial density characteristics for users and satellites, modeling them as point processes and evaluating. In [14], the authors proposed a network architecture where a multi-antenna terrestrial base station and LEO satellite collaborate to provide coverage for both near-shore and off-shore users. In this work, they addressed the dynamicity of the maritime channels by proper modeling of the sea-wave-induced channel variations, and employing robust beamforming. In [15], the authors studied the power allocation problem for a hybrid satellite-UAVs-terrestrial network setup, and addressed the channel dynamicity problem by adopting large-scale CSI. Along similar lines, in [16], the authors address the service demands heterogeneity challenge by employing a hybrid non-terrestrial -terrestrial setup and maximizing the minimum ergodic rate for high-priority users whilst maintaining interference below a certain threshold for standard users.

These studies address critical maritime communication challenges, including robust beamforming under dynamic maritime channels, non-orthogonal multiple access for near-shore coverage, and prioritized resource allocation for different user classes. While these integrated approaches extend coverage significantly, they often face challenges in providing cost-effective, flexible solutions with high data rates.

UAV-based solutions have emerged as a particularly promising component for maritime communications due to their flexibility and ability to provide on-demand coverage. These approaches have gained significant attention in numerous research studies [17], establishing themselves as a key non-terrestrial connectivity option. In [18], the authors propose three different architectures for the deployment of a single UAV-aided relaying solution for maritime - terrestrial connectivity to address large container vessels blockages. Many recent contributions have been devoted to investigating the incorporation of RISs with UAV supported maritime networks [19]–[21]. In [19], the authors adopt reinforcement learning to maximize the overall system's long-term uplink energy efficiency of a terrestrial maritime communication system supported by a RIS-equipped-UAV, under malicious jamming. Towards this aim, the power allocation at the terrestrial base station, both active and passive RIS elements phase and the active/passive elements splitting ratio are tuned while maintaining a pre-determined minimum signal-to-interference-plus-noise (SINR) ratio for the maritime users. In [20], the authors consider aerial-RIS-supported martime communications to counteract the terrestrial link blockage. Towards this end, RIS elements are tuned, to maximize the overall system achievable rate based on the channel state information (CSI) values estimated through the proposed two-phase channel estimation protocol therein. Along similar lines, in [21], the authors exploit deep reinforcement learning to maximize the long-term energy efficiency of a multi-user maritime communications system comprised of a terrestrial base station and a RIS-equipped UAV. The UAV placement, energy harvesting phase time portion, RIS reflection coefficients, and transmitter beamforming are optimized. While RIS integration enhances signal quality, optimizing UAV movement patterns presents another critical dimension for maritime communications.

Beyond basic UAV deployment, trajectory optimization is critical for maximizing the effectiveness of UAV-aided maritime networks [22]–[27]. Recent studies have addressed diverse maritime communication scenarios including: maximizing ships' secrecy rates in the presence of eavesdroppers [25], optimizing multiple relaying UAVs to extend terrestrial coverage for mobile vessels [28], coordinating multiple UAVs serving as relays between terrestrial and satellite networks [26], and enhancing emergency maritime communications [29]. An innovative approach involves tethered UAVs positioned both onshore and onboard ships to provide sustainable extended offshore coverage [30]. Despite these advances, UAV-based maritime solutions face significant limitations: conventional UAVs suffer from limited endurance due to battery constraints, while tethered UAVs, though offering extended operation time, are severely restricted in their mobility and deployment locations. These constraints create a challenge in maritime communications where both endurance and positioning flexibility are simultaneously required.

A promising approach to overcome these limitations is through laser-powered UAV technology, which combines the endurance advantages of tethered UAVs with the positioning flexibility of conventional UAVs. This technology has attracted significant attention [31]–[35] due to its extended flight range and unlimited duration capabilities while maintaining freedom of movement. Research has explored several key directions: optimizing outage and error probabilities for large-scale laser-powered UAV systems [31]; maximizing wireless charging efficiency through 3D placement optimization [32]; enhancing data collection through cluster formation and trajectory planning [33]; joint optimization of UAV placement/trajectory with resource allocation [34],

[35]; and advanced power management strategies including energy allocation, task offloading, and opportunistic rooftop resting [36], [37]. Recent work has also investigated simultaneous wireless information and power transfer [38], [39] and explored laser-powered UAVs as relays [40] or enablers for internet of things (IoT) backscattering networks [41], [42]. However, despite this growing body of research, the application of multi-laser powered UAV swarms specifically for extended offshore coverage remains unexplored. Unlike single laser powered UAV setups, employing multiple lasers to power a swarm entails significant challenges represented in power distribution of laser sources between different swarm elements, which in turn controls their reachable space. In addition, it makes the power reception device design more challenging compared with the single power source case, as multi-directional reception is needed.

To address this gap, we propose the first systematic study of multi-laser powered UAV swarms for extended offshore coverage, combining the flexibility of swarm coordination with laser-sustained operation to enable persistent broadband connectivity in maritime environments. The main contributions of this work towards this aim are summarized as follows:

- Proposing a novel maritime wireless communication architecture where multi-laser powered UAV swarms equipped with hemispherical photoelectric converters provide robust broadband coverage to offshore nodes, eliminating the need for complex tracking systems while ensuring efficient power reception at extended ranges and high angles of incidence.
- Proposing the use of antennas featuring hemispherical radiation pattern onboard offshore ships mounted on gyroscopic mechanical stabilizers to eliminate the specular reflection contribution to the received signal.
- Deriving a comprehensive analytical model for power harvesting efficiency in hemispherical photoelectric converters, enabling accurate prediction of captured optical power from multiple laser sources at varying incident angles and distances for maritime UAV applications.
- Developing a single-block successive convex approximation (SCA) approach to solve the non-convex optimization problem of UAV placement, laser power allocation, and transmission power control. Our solution targets overall and worst-case user spectral efficiency (SE) maximization through novel SCA-compatible bounds for the hemispherical receiver setup and UAV-mounted uniform planar antenna arrays.
- Validating our approach through rigorous simulations with real maritime vessel data, we demonstrate significant improvements in both total spectral efficiency and worst-case user performance compared to benchmark low-complexity solutions and a corresponding tethered UAVs setup.

***Notations*:** In this paper, we represent vectors by small bold letters as $\boldsymbol{a}$, where $\boldsymbol{a} = [a_x\ a_{\mathrm{y}}\ a_z]^{\mathrm{T}}$, with a_x, a_y, and a_z representing its x, y, and z coordinates, respectively, and $(.)^{\mathrm{T}}$ representing the transpose operator. Furthermore, we use $||.||_2$ to denote the ℓ_2-norm, while we use $|.|$ to represent the absolute value of a scalar, or the Lebesgue measure of a set. $\mathbb{I}(C)$ represents an indicator function where $\mathbb{I}(C) = 1$ if the condition C is satisfied and $\mathbb{I}(C) = 0$, otherwise. We use calligraphic fonts to represent symbols for sets. Moreover, we use $\mathrm{F.O.T}[.]$ as an operator that finds the first-order Taylor series expansion of the argument function.

The rest of this paper is organized as follows: first, we detail the considered system and channel models in Section II. Next in Section III, we formulate and solve the system overall spectral efficiency maximization using single-block SCA. We then propose a single-block SCA-based solution of minimum spectral efficiency maximization problem in Section IV. Subsequently, we present extensive set of simulations in Section V. Finally, the paper is concluded in Section VI.

II. System and Channel Models

In this work, we consider a non-terrestrial-aided maritime network consisting of K quasi-stationary maritime users, served by a swarm of rotary wing UAVs consisting of U identical elements. In order to provide uninterrupted and extended offshore coverage, the UAV swarm is remotely charged by L powerful laser sources deployed onshore at fixed locations. The UAVs' locations are denoted by $\boldsymbol{Q}_{\mathbf{u}}$, where the position of the i-th UAV is given by $\boldsymbol{q}_{\boldsymbol{i}}^{\mathbf{U}} \triangleq \left[q_{i,\mathrm{x}}^{\mathrm{U}}\ q_{i,\mathrm{y}}^{\mathrm{U}}\ q_{i,\mathrm{z}}^{\mathrm{U}}\right]^{\mathrm{T}}$. Likewise, the laser sources locations are denoted by $\boldsymbol{Q}_{\mathbf{L}}$, where the location of the i-th laser source is given by the vector $\boldsymbol{q}_{\boldsymbol{i}}^{\mathbf{L}} \triangleq \left[q_{i,\mathrm{x}}^{\mathrm{L}}\ q_{i,\mathrm{y}}^{\mathrm{L}}\ q_{i,\mathrm{z}}^{\mathrm{L}}\right]^{\mathrm{T}}$. We assume that the optical radiated power from each Laser source is split into U directive beams each of which is directed towards one of the UAVs. We further assume that the angular pointing error for all laser beams is limited to θ_{err}.

At the UAVs' side, a photoelectric converter with hemispherical aperture of radius r_{pd} is used to alleviate the need for laser beam tracking at the UAV, with R_{PD} photodetector responsivity. The radiated laser power portion by the ℓ-th laser source dedicated to the i-th UAV is denoted by $P_{i,\ell}^{\mathrm{L}}$, while $\boldsymbol{P}_{\mathbf{L}}$ represents the set of all radiated laser power variables. Furthermore, all the laser sources are assumed identical, featuring a beam-divergence angle of $\Delta\theta$ and initial beam diameter of D_{o}. The maximum optical output power of the considered lasers is denoted by $P_{\mathrm{M}}^{\mathrm{L}}$ and is set according to radiation exposure limits and the laser source output rating. In Fig. 1, we present an example for the considered setup with $L = 2$, $U = 3$, and $K = 5$.

Each UAV is equipped with a uniform planar array of N_{T}-antenna elements, with a carrier frequency f_{c}. In addition, the proposed framework assumes a symmetric orthogonal multiple access scheme, such as time division multiple access (TDMA) with equal time slots, frequency division multiple access (FDMA) with equal bandwidth shares, or

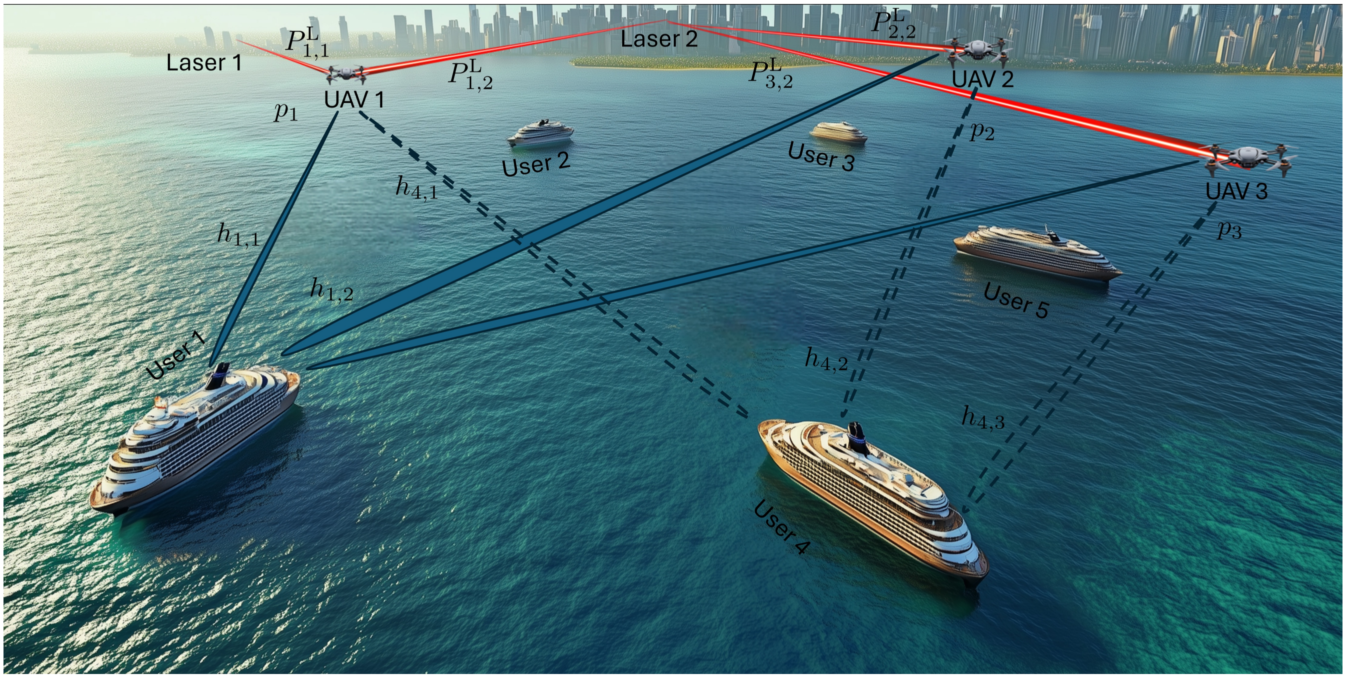

FIGURE 1: Illustration of the multi-laser powered UAV swarm maritime communication system with $L = 2$ laser sources, $U = 3$ UAVs, and $K = 5$ maritime users.

code division multiple access (CDMA) with equal code allocation, all of which yield identical rate expressions under the considered formulation. Accordingly, each UAV employs coherent beamforming to focus the radiated power towards the user determined by the round-robin scheduler. We define the radiated power by the i-th UAV as p_i, while the set of all radiated power variables is denoted by $\boldsymbol{p}$. The radiated power from UAVs at any instant are restricted to exceed a maximum value of $P^{\mathrm{U}}_{\mathrm{M}}$ to comply with radiation exposure limits. Moreover, we assume that each ship is equipped with a receiving antenna featuring a hemispherical radiation pattern. Furthermore, it is assumed that the receiving antenna is mounted on a stabilizing platform with automatic controllers that compensate for the sea waves motion and maintain a horizontal orientation for the receiver with a maximum residual error of $\theta^{\mathrm{err}}_{\mathrm{Stab}}$. In order to harmonize the operation of the UAV swarm, we assume a central controller provides the swarm with synchronization signals to allow for harnessing the gains of the collaborative beamforming [43]. In addition, we assume that the control signaling between the central controller and the swarm elements operates on a separate frequency band to avoid interference with both the access and the backhaul links. We further assume that the backhaul links between the swarm and the central controller are provisioned with sufficient bandwidth to support the maximum aggregate rate that the swarm can deliver to the served users; such bandwidth can be realized through free-space optical communications. The UAV swarm adopts a fly-then-hover strategy, where the hovering locations and the associated laser and UAV power allocations are optimized at every coherence interval. Since only quasi-stationary users are considered, the required propulsion power during the flying phase can be approximated by the UAV hovering power. The practical deployment of the proposed algorithms necessitates optimized software and hardware implementation to ensure that each problem instance is solved within the channel coherence time.

A. CHANNEL MODEL

As for the channel model, we focus in this work on offshore communications with limited communication range, where users are located within a rectangular region with extending L_{R} m over the coastline and W_{R} m normal to the coastline. Accordingly, we assume calm sea conditions, for which the number of multipath reflections between the UAVs and the maritime users is significantly reduced. It is reported in [44] that for low altitude communications, the two-ray channel model best describes path loss for air-to-sea links in 86% of the cases in the conducted measurement campaign, while 95% of the cases are best described by the three-ray model. It is worth mentioning, that Rician and Rayleigh small fading models are suitable for high-state sea level [45]. The adoption of two-ray/ three-ray model depends on the communications range and a threshold distance called d_{break}, expressed as [46]

$$d_{\mathrm{break}} = \frac{4h_{\mathrm{R}}h_{\mathrm{T}}}{\lambda}, \tag{1}$$

where h_{R} and h_{T}, represent the receiver, and the transmitter heights, respectively, while λ represents the transmission wavelength. Assuming a minimum UAV height of 40 m above the sea surface and receiver antenna height of 5 m on the ship, the break distance varies between 16 and 21 Kms for radio transmission over frequencies between $6-8$ GHz. In this study, the region of interest is a 10 Km × 10 Km, hence, the maximum UAV-user separation distance does not exceed d_{break}. Accordingly, the third ray reflected from the ducting layer can be neglected. In addition, the ships' receiver position above sea level, along with horizontal orientation maintenance via stabilizer, and the hemispherical receiving antenna gain ensures that the specular reflection from the sea will not contribute to the received signal under the condition that $\tan^{-1}(z^{\text{U}}_{\text{min}}/\sqrt{L_{\text{R}}^2+W_{\text{R}}^2}) \geq \theta^{\text{err}}_{\text{Stab}}$, where $z^{\text{U}}_{\text{min}}$ represents the UAV minimum permissible altitude. The coherence time of a link between a UAV and a ship can be approximated by the inverse of the Doppler spread, and is expressed as

$$T_{\text{c}} = \frac{1}{2v|\cos(\theta)|}\frac{c}{f_{\text{c}}}, \tag{2}$$

where v denotes the ship speed, θ is the angle the ship's velocity vector and the line connecting the UAV to the ship, and c is the speed of light. For fishing trips and scenic cruising, v ranges from 1 to 5 knots; hence, the worst-case coherence time for the maritime carrier frequencies of 6 to 8 GHz is approximately 7 to 48 ms.

Consequently, the channel model adopted in this work is a deterministic pathloss power-law model.

In such a setup, the received signal by the i-th user at its dedicated time slot is given by

$$y_i = \sum_{\ell=1}^{U} h_{i,\ell}\sqrt{p_\ell}s_i + n_i, \tag{3}$$

where $h_{i,\ell}$ represents the channel gain coefficient between the ℓ-th UAV and the i-th user, s_i is the transmitted symbol to the i-th user, and n_i denotes the additive white Gaussian noise arising at the receiver circuitry. It is worth mentioning that n_i follows a complex circularly symmetric Gaussian distribution with zero mean and σ_{n}^2 variance. Based on the previously mentioned channel model assumptions, the channel gain coefficient can be expressed as

$$h_{i,\ell} = \sqrt{\left(\frac{c}{4\pi f_{\text{c}}}\right)^2 \frac{1}{d_{i,\ell}^{\gamma}} G_{\text{T},i,\ell} G_{\text{R}} e^{-j\frac{2\pi d_{i,\ell}}{\lambda}}}, \tag{4}$$

where c represents the speed of light in free space, $d_{i,\ell}$ is the distance between the ℓ-th UAV and the i-th user, γ is the path loss exponent, and G_{R} represents the antenna gain at all users measured along the direction of all the transmitters. $G_{\text{T},i,\ell}$ represents the antenna gain of the ℓ-th UAV antenna measured along the direction pointing to the i-th user and is expressed as

$$G_{\text{T},i,\ell} = N_{\text{T}}^2\left(\frac{q^{\text{u}}_{\ell,\text{z}}}{d_{i,\ell}}\right)^{\zeta}, \tag{5}$$

[47] where ζ determines the transmitting antenna directivity. It is worth mentioning that the fraction $\frac{q^{\text{u}}_{\ell,\text{z}}}{d_{i,\ell}}$ represents cosine the angle between the normal to the antenna array of the ℓ-th UAV and the line joining the center of the array and the i-th user.

B. HARVESTED POWER USING A HEMISPHERICAL PHOTOELECTRIC CONVERTER APERTURE

Before defining the operation optimization problem, we first establish key performance metrics. Accordingly, we start with the total power harvested at the i-th UAV from all laser sources, expressed as [48, Eq. 2.21]

$$P_i^{\text{H}} = 0.75 v_{\text{t}} x_i \ln\left(1+\frac{x_i}{I_o}\right), \tag{6}$$

where x_i represents the photoelectric current generated at the i-th UAV photoelectric converter, and I_{o} represents the dark saturation current. Since each UAV is being charged from all the laser sources, x_i is the generated current due to the superposition of all incident laser beams. Consequently, x_i can be expressed as

$$x_i = R_{\text{PD}}\sum_{\ell=1}^{L} P^{\text{opt}}_{i,\ell}, \tag{7}$$

where $P^{\text{opt}}_{i,\ell}$ represents the captured optical power at the i-th UAV from the ℓ-th laser source. Given that the distances between the UAVs and the laser sources are much larger than the photoelectric converter dimensions, the power density variations over the converter area become negligible and all incident rays on the aperture can be treated as parallel [49]. Notably, the resulting harvested energy approximation error does not exceed 0.5% for all separation distances considered in this work. Consequently, $P^{\text{opt}}_{i,\ell}$ can be expressed in terms of the effective area of the photoelectric converter at the i-th UAV as perceived from the ℓ-th laser location, $A^{\text{eff}}_{i,\ell}$, and the laser power density due to the ℓ-th laser source beam at the i-th UAV as

$$P^{\text{opt}}_{i,\ell} \approx A^{\text{eff}}_{i,\ell} P^{\text{d}}_{i,\ell}. \tag{8}$$

For a Gaussian laser beam in a far-field setting, $P^{\text{d}}_{i,\ell}$ can be expressed as [49]

$$P^{\text{d}}_{i,\ell} = P^{\text{L}}_{i,\ell} e^{-8\left(\frac{\theta_{\text{err}}}{\Delta\theta}\right)^2} \frac{e^{-\alpha d^{\text{L}}_{i,\ell}}}{\left(D_o + \Delta\theta d^{\text{L}}_{i,\ell}\right)^2}, \tag{9}$$

where

$$\alpha = \alpha_{\text{c}} + \alpha_{\text{s}}, \tag{10}$$

and

$$\alpha_{\text{s}} = 0.2\ln(10)\sqrt{23.17\left(\frac{2\pi}{\lambda_{\text{L}}}\right)^{\frac{7}{6}} C_{\text{n}}^2}, \tag{11}$$

where α represents the overall laser beam attenuation coefficient due to absorption, scattering and scintillation, while $d^{\text{L}}_{i,\ell}$ denotes the distance between the i-th UAV and the ℓ-th laser source. In addition, α_{c} is the extinction coefficient, α_{s} denotes the scintillation exponent, λ_{L} represents the laser beam wavelength and C_{n}^2 resembles the atmospheric turbulence coefficient. It is worth mentioning that angular pointing errors of microradians and sub-microradians are attainable using gimbals, moving mirrors and hybrid structures constituting of both [50].

Recalling that the effective area of an aperture is the equivalent orthogonal area to the impinging radiation direction, that captures the same amount of power, as depicted in Fig. 2. By projecting the hemisphere area onto the plane orthogonal to the line joining the centers of the i-th UAV and the ℓ-th laser source, $A^{\mathrm{eff}}_{i,\ell}$ can be expressed as

$$A^{\mathrm{eff}}_{i,\ell} = \frac{\pi r^2_{\mathrm{PD}}}{2}\left(1 + \frac{q^{\mathrm{U}}_{i,\mathrm{z}} - q^{\mathrm{L}}_{\ell,\mathrm{z}}}{d^{\mathrm{L}}_{i,\ell}}\right). \tag{12}$$

C. HEMISPHERICAL VS FLAT PHOTOELECTRIC CONVERTERS FOR LASER POWERED UAVs

In this section, we highlight the advantages of employing hemispherical apertured photoelectric converters in laser powered UAVs. Firstly, we classify the employed energy receivers that could serve this purpose into two categories, static and dynamic receivers. In dynamic systems, energy transmission performance is optimized when the normal to the aperture aligns with the line joining the transmitter and the receiver, in such case the effective aperture area matches the physical aperture. To achieve this gain, this alignment comes at the cost of adding pointing and tracking system onboard the UAV which adds significant system complexity and questions the overall charging efficiency as the UAV weight increases, and the needed propulsion power in turn. Consequently, it is favorable to install a static energy receiver onboard UAV to alleviate the alignment burden, which reduces to that on the transmitter side.

The geometric configuration of the receiver aperture is crucial as it directly determines the effective collection area across various incidence angles, thereby significantly impacting the overall charging efficiency of the system. We consider two cases, namely, a fixed flat horizontal aperture patched to the UAV's bottom, and a hemispherical aperture. To compare these cases, we plot the effective aperture area of both geometries given identical physical aperture area of 1 cm^2. As shown in Fig. 3, for angles of incidence below 70° approximately, the flat surface receiver dominates; however, it fails severely when the angle of incidence approaches 90°. On the other hand, the hemispherical receiver maintains a minimum effective area equivalent to a quarter of the physical area, ensuring reasonable efficiency at high angles of incidence. Therefore, understanding the typical operating angles of incidence is critical when designing laser-powered UAV systems. A key advantage of laser-powered UAVs is their capability to operate at extended distances from the charging source while maintaining continuous flight. However, these systems typically operate within a limited range of permissible altitudes due to safety and operational constraints. In Fig. 4, we plot the effective areas of both receiving apertures as the horizontal distance increases between the UAV and the laser source while it maintains a constant height. The three plotted curves per receiving architecture represent the set of heights $100, 300, 500$ m. It is clearly observed that even for 500 m height, the hemispherical receiver provides significant gains at 2 km horizontal distance and beyond. Hence, for the operational regions of interest in maritime laser-powered UAV applications – particularly at extended horizontal distances beyond 2 km – hemispherical receivers are highly recommended due to their superior performance at the inevitable high angles of incidence.

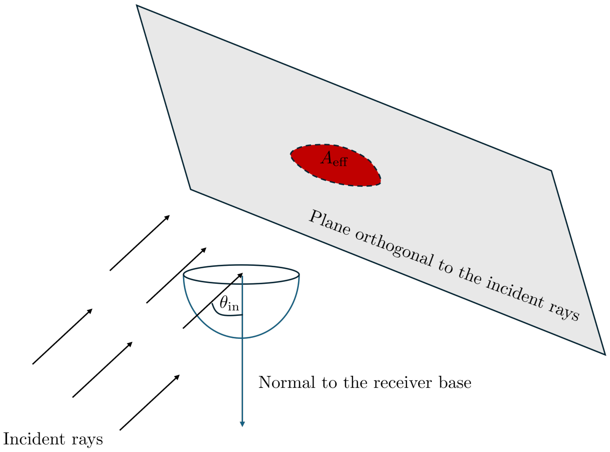

FIGURE 2: Geometry of the effective area of the photoelectric converter

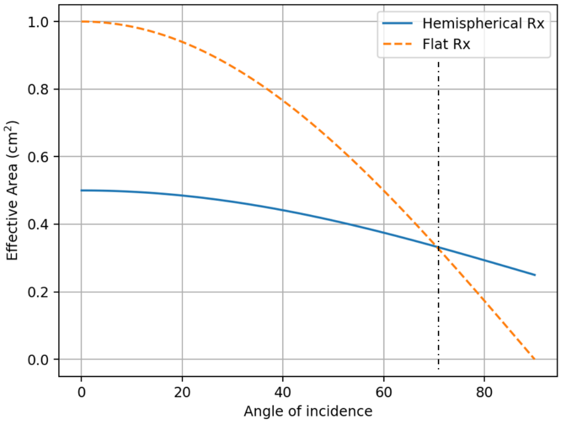

FIGURE 3: Effective area of the photoelectric converter vs angle of incidence.

III. Overall System Spectral Efficiency Maximization

The lack of broadband terrestrial coverage, coupled with the large link latency and limited bandwidth offered by satellite constellations, highlights the need for aerial platform-based wireless coverage. This work adopts spectral efficiency as the primary performance metric, which directly captures the physical layer capacity under the proposed optimization framework. Coverage fairness is addressed through the

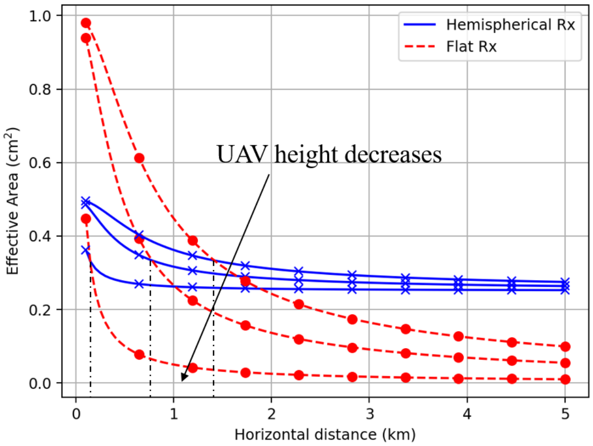

FIGURE 4: Effective area of the photoelectric converter vs horizontal distance between UAV and laser source at different fixed heights.

worst-case SE formulation presented in the next section. Cross-layer metrics such as latency and reliability, which depend on traffic characteristics and protocol design, are identified as directions for future work. In this section, we study the network overall spectral efficiency maximization problem for the considered laser-powered UAV swarm setup while maintaining a minimum quality-of-service for users experiencing inferior channels. We focus on optimizing UAVs locations, power allocation, and power distribution among the UAV swarm.

It is well-known that the capacity achieving distribution for s_i is the proper complex Gaussian distribution [51]. Consequently, the overall average spectral efficiency for the considered setup when Gaussian codebook is adopted is expressed as:

$$R = \sum_{i=1}^{K} R_i, \tag{13}$$

with R_i is defined as:

$$R_i = \frac{1}{K}\log_2\left(1 + \frac{\beta_o}{\sigma_{\mathrm{n}}^2}\sum_{\ell=1}^{\mathrm{U}} \frac{p_\ell}{d_{i,\ell}^{\gamma}}\left(\frac{q^{\mathrm{u}}_{\ell,\mathrm{z}}}{d_{i,\ell}}\right)^{\zeta}\right), \tag{14}$$

where $\beta_o = \left(\frac{c}{4\pi f_c}\right)^2 N_{\mathrm{T}}^2 G_{\mathrm{R}}$. The overall spectral efficiency maximization can then be formally defined as:

$$(\mathbf{P1}) \qquad \max_{\boldsymbol{Q}_{\mathrm{u}}, \boldsymbol{P}_{\mathrm{L}}, \boldsymbol{p}} \qquad R$$

Subject to

$$\mathrm{C1}: ||\boldsymbol{q}^{\mathrm{u}}_i - \boldsymbol{q}^{\mathrm{u}}_j||_2 \geq d^{\mathrm{c}}_{\min}, \qquad \forall (i,j) \in \{1,..,U\}^2,\ i \neq j$$

$$\mathrm{C2}: \sum_{i=1}^{\mathrm{U}} P^{\mathrm{L}}_{i,\ell} \leq P^{\mathrm{L}}_{\mathrm{M}}, \quad \forall \ell \in \{1,\ldots,L\}$$

$$\mathrm{C3}: P_{\mathrm{Hov}} + p_i \leq P^{\mathrm{H}}_i, \quad \forall i \in \{1,\ldots,U\}$$

$$\mathrm{C4a}: z^{\mathrm{U}}_{\min} \leq q^{\mathrm{U}}_{i,\mathrm{z}} \leq z^{\mathrm{U}}_{\max}, \quad \forall i \in \{1,\ldots,U\}$$

$$\mathrm{C4b}: -L_{\mathrm{R}}/2 \leq q^{\mathrm{U}}_{i,\mathrm{x}} \leq L_{\mathrm{R}}/2, \quad \forall i \in \{1,\ldots,U\}$$

$$\mathrm{C4c}: 0 \leq q^{\mathrm{U}}_{i,\mathrm{y}} \leq W_{\mathrm{R}}, \quad \forall i \in \{1,\ldots,U\}$$

$$\mathrm{C5}: R_i \geq R_{\min,i} \qquad \forall i \in \{1,\ldots,K\}$$

$$\mathrm{C6}: p_i \leq P^{\mathrm{U}}_{\mathrm{M}} \qquad \forall i \in \{1,\ldots,U\},$$

where $d^{\mathrm{c}}_{\min}$ represents the minimum acceptable inter-separation distance between any two UAVs, P_{Hov} is the needed propulsion power to keep the UAV hovering, $z^{\mathrm{U}}_{\max}$ denote the maximum permissible UAV altitude, respectively. The semantics of the constraints are as follows. C1 enforces a minimum separation distance between any pair of UAVs for collision avoidance purpose. C2 guarantees that the total radiated power from any laser source does not exceed the maximum permissible value. C3 ensures that the harvested power by each UAV caters for its hovering and transmission power needs. Note that the needed propulsion power does not depend due to static positioning of the UAVs, for non-stationary UAVs the propulsion power should account for the UAVs velocity as indicated in [52]. C4 defines the feasibility region for UAVs deployment locations. C5 provides a customized minimum quality-of-service guarantee for each user. Finally, C6 imposes a maximum radiated power over all the UAVs to avoid radiation over-exposure.

The non-convexity of the previous problem is obvious due to the objective function, C1, C3, and C5. By introducing the set of slack variables $\Gamma_{i,\ell},\ \forall (i,\ell) \in \mathcal{U} \triangleq \{1,\ldots,K\} \times \{1,\ldots,U\}$, we get the following equivalent problem,

$$(\mathbf{P2}) \qquad \max_{\boldsymbol{Q}_{\mathrm{u}}, \boldsymbol{P}_{\mathrm{L}}, \boldsymbol{p}, \boldsymbol{\Gamma}} \qquad \frac{1}{K\ln(2)}\sum_{i=1}^{K}\ln\left(1 + \frac{\beta_o}{\sigma_{\mathrm{n}}^2}\sum_{\ell=1}^{U}\Gamma_{i,\ell}\right)$$

Subject to

$$\mathrm{C1} - \mathrm{C4}, \mathrm{C6},$$

$$\widetilde{\mathrm{C5}}: 1 + \frac{\beta_o}{\sigma_{\mathrm{n}}^2}\sum_{\ell=1}^{U}\Gamma_{i,\ell} \geq e^{K\ln(2)R_{\min,i}} \qquad \forall i \in \{1,\ldots,K\},$$

$$\mathrm{C7}: \frac{p_\ell}{d_{i,\ell}^{\gamma}}\left(\frac{q^{\mathrm{u}}_{\ell,\mathrm{z}}}{d_{i,\ell}}\right)^{\zeta} \geq \Gamma_{i,\ell}, \qquad \forall (i,\ell) \in \mathcal{U}.$$

It is observed that adding the slack variables resolved the non-convexity of the objective function and C5, which is replaced by its equivalent $\widetilde{\mathrm{C5}}$, leaving only the non-convexity in C3 and the added constraint C7. Taking the logarithm of both sides of C7, re-arranging terms, and approximating C1 with a smooth minimum function to simplify the feasibility region, we get

$$(\mathbf{P3}) \qquad \max_{\boldsymbol{Q}_{\mathrm{u}},\boldsymbol{P}_{\mathrm{L}},\boldsymbol{p},\boldsymbol{\Gamma}} \qquad \frac{1}{K\ln(2)}\sum_{i=1}^{K}\ln\left(1+\frac{\beta_o}{\sigma_{\mathrm{n}}^2}\sum_{\ell=1}^{U}\Gamma_{i,\ell}\right)$$

Subject to

$$\mathrm{C2}-\mathrm{C4}, \widetilde{\mathrm{C5}}, \mathrm{C6},$$

$$\widetilde{\mathrm{C1}}: -\frac{1}{\bar{\alpha}}\mathrm{LSE}(-\{\bar{\alpha}d_{i,j}\}_{\forall(i,j)\in\mathcal{K}}) - \frac{1}{\bar{\alpha}}\ln\left(\frac{2}{U^2-U}\right) \geq d_{\min}^{\mathrm{c}},$$

$$\widetilde{\mathrm{C7}}: \zeta\ln(q_{\ell,\mathrm{z}}^{\mathrm{u}}) + \ln(p_\ell) - (\gamma+\zeta)\ln(d_{i,\ell}) \geq \ln(\Gamma_{i,\ell}),\ \forall(i,\ell)\in\mathcal{U},$$

where $\bar{\alpha}$ is a parameter that controls the accuracy of the smooth minimum function approximation[1], $\mathrm{LSE}(\boldsymbol{x})$ represents the log-sum-exponential function, i.e., defined as $\mathrm{LSE}(\boldsymbol{x}) = \ln\sum_i e^{x_i}$. $\mathcal{K}$ denotes the set of distinct UAV pairs defined as $\mathcal{K} = \{(i,j) : (i,j) \in \{1,\ldots,U\}^2, i<j\}$.

In the previous formulation, the non-convex terms are now limited to the harvested power in $\widetilde{\mathrm{C3}}$, the L.H.S of $\widetilde{\mathrm{C1}}$, and the distance logarithm term in $\widetilde{\mathrm{C7}}$. This problem can be solved iteratively using SCA with the following kernel convex optimization problem to get a Karush-Kuhn-Tucker (KKT) point as shown in $\overline{\mathrm{C7}}$

$$(\mathbf{P4}) \qquad \max_{\boldsymbol{Q}_{\mathrm{u}},\boldsymbol{Q}_{\mathrm{L}}\boldsymbol{P}_{\mathrm{L}},\boldsymbol{p},\boldsymbol{\Gamma}} \qquad \frac{1}{K\ln(2)}\sum_{i=1}^{K}\ln\left(1+\frac{\beta_o}{\sigma_{\mathrm{n}}^2}\Gamma_i\right)$$

Subject to

$$\mathrm{C2}, \mathrm{C4}, \widetilde{\mathrm{C5}}, \mathrm{C6},$$

$$\overline{\mathrm{C1}}: -\frac{1}{\bar{\alpha}}\mathrm{LSE}(-\{\bar{\alpha}\mathrm{F.o.T}\,[d_{i,j}]\}_{\forall(i,j)\in\mathcal{K}}) - \frac{1}{\bar{\alpha}}\ln\left(\frac{2}{U^2-U}\right) \geq d_{\min}^{\mathrm{c}},$$

$$\widetilde{\mathrm{C3}}: P_{\mathrm{Hov}} + p_i \leq \tilde{P}_i^{\mathrm{H}}, \quad \forall i\in\{1,\ldots,U\}$$

$$\overline{\mathrm{C7}}: \zeta\ln(q_{i,\mathrm{z}}^{\mathrm{U}}) + \ln(p_\ell) \geq \ln(\Gamma_{i,\ell}) + (\gamma+\zeta) \times\left(\ln(d_{i,\ell,o}) + \frac{d_{i,\ell}-d_{i,\ell,o}}{d_{i,\ell,o}}\right),\ \forall(i,\ell)\in\mathcal{U}$$

The transition from $(\mathbf{P3})$ to $(\mathbf{P4})$ is realized by finding an SCA-compatible bound for the L.H.S of C1 to get $\overline{\mathrm{C1}}$, replacing P_i^{H} in C3 with the SCA-compatible concave lower bound $\tilde{P}_i^{\mathrm{H}}$ to get $\widetilde{\mathrm{C3}}$, and upper bounding the distance logarithm term in $\widetilde{\mathrm{C7}}$ with an SCA comptible convex upper bound to get $\overline{\mathrm{C7}}$.

In the L.H.S of $\widetilde{\mathrm{C1}}$ the LSE function is convex and increasing in all the input variables. By upper bounding its arguments using their first-order Taylor approximations, the L.H.S of $\widetilde{\mathrm{C1}}$ is lower bounded with the concave SCA-compatible lower bound appearing in the L.H.S of $\overline{\mathrm{C1}}$. As for $\widetilde{\mathrm{C3}}$, we provide the derivation in appendix A. Finally, $\overline{\mathrm{C7}}$ by upper bounding the logarithm function with its first order Taylor approximation, hence an SCA-compatible convex upper bound is reached for the R.H.S of $\widetilde{\mathrm{C7}}$.

Finally, the proposed solution of (P3) is summarized in Algorithm I, where starting with a feasible initial point, an iterative process starts where an instance of (P4) is constructed based on the solution provided by the previous iteration and solved using an interior point method. Then, the process repeats until the algorithm converges.

Algorithm I: Overall Spectral Efficiency Maximization

```
Initialize $\boldsymbol{Q}_{\mathrm{u}}^o, \boldsymbol{P}_{\mathrm{L}}^o, \boldsymbol{p}^o, \boldsymbol{\Gamma}^o$ , Relative Error
while Relative Error $\geq \epsilon_r$ do
    Solve $(\mathbf{P4})$ for $\boldsymbol{Q}_{\mathrm{u}}$, $\boldsymbol{Q}_{\mathrm{L}}$, $\boldsymbol{P}_{\mathrm{L}}$, $\boldsymbol{p}$, $\boldsymbol{\Gamma}$ via interior point method.
    Relative Error $\leftarrow \left|\frac{R-R_o}{R_o}\right|$
    $\boldsymbol{Q}_{\mathrm{u}}^o \leftarrow \boldsymbol{Q}_{\mathrm{u}}$, $\boldsymbol{P}_{\mathrm{L}}^o \leftarrow \boldsymbol{P}_{\mathrm{L}}$, $\boldsymbol{p} \leftarrow \boldsymbol{p}^o$, $\boldsymbol{\Gamma} \leftarrow \boldsymbol{\Gamma}^o$
end while
```

The overall iteration complexity of Algorithm I is $\mathcal{O}(I_{\mathrm{SCA}}(U(4+L+K))^{3.5})$, where I_{SCA} represents the number of SCA iterations required for convergence.

IV. Fair user rate maximization

An alternative objective to optimize is the worst-case user communication rate. This metric is crucial to assess the system performance limits from a user oriented perspective and promotes fairness among users in an end-to-end service terms. In addition, solving the system overall spectral efficiency maximization problem through the proposed approach, an initial feasible point is needed. However, finding such a point is neither trivial nor guaranteed due to the finite power budget offered by the laser sources, the maximum allowable radiated power levels, and the minimum quality-of-service requirement for each user. Consequently, we solve minimum spectral efficiency maximization problem to assess the feasibility of (P1) and utilize its solution as an initial feasible guess for (P1).

$$(\mathbf{P5}) \qquad \max_{\boldsymbol{Q}_{\mathrm{u}},\boldsymbol{P}_{\mathrm{L}},\boldsymbol{p}} \quad \min_i\ R_i$$

Subject to

$$\mathrm{C1}-\mathrm{C6}.$$

We reformulate problem (P5) as an equivalent problem $(\widetilde{\mathbf{P5}})$ by introducing an auxiliary variable t to represent the minimum spectral efficiency across all users, thereby transforming the min-max structure into a standard maximization problem with additional constraints:

$$(\widetilde{\mathbf{P5}}) \qquad \max_{\boldsymbol{Q}_{\mathrm{u}},\boldsymbol{P}_{\mathrm{L}},\boldsymbol{p}} \quad t$$

Subject to

$$\mathrm{C1}-\mathrm{C4}, \mathrm{C6},$$

$$\mathrm{C8}: R_i \geq t \qquad \forall i\in\{1,\ldots,K\}.$$

By using the same slack variables set $\boldsymbol{\Gamma}$, and following a similar minimum UAV inter distance approximation, as in $(\mathbf{P3})$, $(\widetilde{\mathbf{P5}})$ can be approximated as

---

[1] as $\bar{\alpha}$ increases, the L.H.S of $\widetilde{\mathrm{C1}}$ approaches the mininmum inter-separation distance between all the UAVs.

$$(\overline{\mathbf{P5}}) \qquad \max_{\boldsymbol{Q}_{\mathrm{u}},\boldsymbol{P}_{\mathrm{L}},\boldsymbol{p},\boldsymbol{\Gamma}} \quad t$$

Subject to

$$\widetilde{\mathrm{C1}}, \mathrm{C2}-\mathrm{C4}, \mathrm{C6}, \widetilde{\mathrm{C7}},$$

$$\widetilde{\mathrm{C8}} : 1+\frac{\beta_o}{\sigma_{\mathrm{n}}^2}\sum_{\ell=1}^{U}\Gamma_{i,\ell} \geq e^{tK\ln(2)} \qquad \forall i \in \{1,\dots,K\}.$$

The similarity between, $(\overline{\mathbf{P5}})$ and $(\mathbf{P3})$ in terms of non-convex terms is evident. Hence, solving $(\overline{\mathbf{P5}})$ for a KKT point can be achieved through SCA. Towards this aim, $(\mathbf{P6})$ is used as the kernel convex optimization problem that utilizes the same previously derived SCA compatible bounds as detailed in Algorithm II

$$(\mathbf{P6}) \qquad \max_{\boldsymbol{Q}_{\mathrm{u}},\boldsymbol{P}_{\mathrm{L}},\boldsymbol{p},\boldsymbol{\Gamma}} \quad t$$

Subject to

$$\overline{\mathrm{C1}}, \mathrm{C2}, \widetilde{\mathrm{C3}}, \mathrm{C4}, \mathrm{C6}, \overline{\mathrm{C7}}, \widetilde{\mathrm{C8}}.$$

Algorithm II: Minimum Spectral Efficiency Maximization

```
Initialize $\boldsymbol{Q}_{\mathrm{u}}^o, \boldsymbol{Q}_{\mathrm{L}}^o \boldsymbol{P}_{\mathrm{L}}^o, \boldsymbol{p}^o, \boldsymbol{\Gamma}^o$ , Relative Error
while Relative Error $\geq \epsilon_{\mathrm{r}}$ do
    Solve $(\mathbf{P6})$ for $\boldsymbol{Q}_{\mathrm{u}}$, $\boldsymbol{Q}_{\mathrm{L}}$, $\boldsymbol{P}_{\mathrm{L}}$, $\boldsymbol{p}$, $\boldsymbol{\Gamma}$ via interior point method.
    Relative Error $\leftarrow \left|\frac{t-t_o}{t_o}\right|$
    $\boldsymbol{Q}_{\mathrm{u}}^o \leftarrow \boldsymbol{Q}_{\mathrm{u}}$, $\boldsymbol{Q}_{\mathrm{L}}^o \leftarrow \boldsymbol{Q}_{\mathrm{L}}$, $\boldsymbol{P}_{\mathrm{L}}^o \leftarrow \boldsymbol{P}_{\mathrm{L}}$, $\boldsymbol{p}^o \leftarrow \boldsymbol{p}$, $\boldsymbol{\Gamma} \leftarrow \boldsymbol{\Gamma}^o$
end while
```

In Algorithm II, $(\overline{\mathbf{P5}})$ is solved iteratively by solving instances of $(\mathbf{P6})$ formulated using the previous SCA iteration solution of $(\mathbf{P6})$ and this process is repeated until the relative error of the minimum spectral efficiency becomes smaller than a given threshold. It is noted that Algorithm II incurs iteration complexity of $\mathcal{O}(I_{\mathrm{SCA},2}(U(4+L+K)+1)^{3.5})$. It is worth mentioning that the convergence of Algorithm I and Algorithm II to a KKT point is guaranteed [53, 2.1.2], featuring a non-decreasing sequence of the objective functions values.

A. FEASIBILITY OF THE FAIR USER RATE MAXIMIZATION PROBLEM

Looking into the constraints of $(\mathbf{P5})$, it is observed that feasibility is not guaranteed. In other words, $(\mathbf{P5})$ can be declared feasible or not based on the number of laser sources used, their placement, their maximum output power, the number of UAVs comprising the swarm and their hovering power, and their minimum inter-separation distance and minimum laser-UAVs separation distance, and their hovering powers. Specifically, feasibility can be assessed by solving the minimum harvested power maximization problem. The problem is deemed feasible if and only if the optimal solution to $(\mathbf{P7})$ yields a minimum harvested power that meets or exceeds the hovering power requirement (i.e., if optimal $\min P_i^{\mathrm{H}} \geq P_{\mathrm{Hov}}$). Otherwise, insufficient energy harvesting capacity renders the original problem infeasible, regardless of other parameter configurations. This may be expressed as:

$$(\mathbf{P7}) \qquad \max_{\boldsymbol{Q}_{\mathrm{u}},\boldsymbol{P}_{\mathrm{L}}} \quad \min_{i} \; P_i^{\mathrm{H}}$$

Subject to

$$\mathrm{C1}-\mathrm{C2}, \mathrm{C4}\;\mathrm{C6},$$

$$\bar{\mathrm{C}}3 : P_{\mathrm{Hov}} \leq P_i^{\mathrm{H}}, \quad \forall i \in \{1,\dots,U\}.$$

This problem is non-convex, hence, we solve it using single-block SCA by exploiting the previously derived bound for harvested power where the following kernel convex optimization problem is used,

$$(\mathbf{P8}) \qquad \max_{\boldsymbol{Q}_{\mathrm{u}},\boldsymbol{P}_{\mathrm{L}}} \quad t$$

Subject to

$$\overline{\mathrm{C1}}, \mathrm{C2}, \mathrm{C4}\;\mathrm{C6},$$

$$\overline{\mathrm{C3}} : t \leq \tilde{P}_i^{\mathrm{H}}, \quad \forall i \in \{1,\dots,U\}.$$

V. Simulation Results

In this section, we evaluate the performance of the proposed algorithms for operation optimization of multi-laser powered UAV swarm as it serves a multitude of offshore users. Towards this end, we adopt a fixed users layout over all the conducted simulations where user locations are adopted from the average locations over the first 5 seconds of the 23rd hour of the recorded ships AIS data on January 1st, 2024 [54] within a square region where L_{R}= 10 Km and W_{R}= 10 Km along the western coast of USA. The users cartesian coordinates along with their associated longitudes and latitudes are provided in Table 1, and their layout is shown along with our placement solutions in Fig. 5. We assume the lasers are uniformly deployed over 1 km distance along the x-axis, 500 m away from the shore centered about the location vector $\boldsymbol{q}_{\mathrm{L}}^{\mathrm{c}} = [q_{\mathrm{L}}^{\mathrm{c}} \quad 0 \quad 5]^{\mathrm{T}}$. In the considered simulations, we employ a unified minimum rate requirement $(R_{\min})$ for all users, i.e., $R_{\min,i} = R_{\min}$ and the value for $R_{\min}$ is set to 95% of the minimal value for the maximized fair user spectral efficiency over the swept simulation parameter values. Unless otherwise stated, we use the default setup parameters values provided in Table 2, where the chosen values are based on [34], [35], [42], [55]–[57].

In the sequel, we assess the performance of our proposed total SE maximization (the SESCA), and worst-case user SE maximization (the WSESCA) solutions. Towards this aim, we compare their performance against the initial provided solution to the SCA algorithms (SEI). In addition, we consider another setup where a battery-powered swarm is used, for which we denote the total SE maximization solution by ”SEBSCA” and the worst-case SE maximization by "WSEBSCA". It is worth mentioning that the battery powered solutions are obtained using Algorithm I and II using $\lim_{x\to\infty} P_{\mathrm{M}}^{\mathrm{L}} = x$. Moreover, we extend the performance comparison to include tethered UAV swarm, for which, we assume the same swarm size, all the tether are hooked to the same point on land given by the location vector $\boldsymbol{q}_{\mathrm{T}}^{\mathrm{c}} = [q_{\mathrm{L}}^{\mathrm{c}} \quad 0 \quad 0]^{\mathrm{T}}$. All the tethered UAVs have the same tether length L_{T} which is set to 200 m. For the tethered setup, we present the total SE maximization solution denoted by "SETSCA" and the worst-case SE maximization solution denoted by "WSETSCA". It is worth mentioning that both SETSCA and WSETSCA solutions are based on the algorithms I and II, respectively, with an added constraint on the distances between the UAVs and the tethers anchor due to limited tether length, and by relaxing the power budget constraints. For the SETSCA and the WSETSCA, the optimization parameters are the UAVs locations only, since the optimal transmit power is dictated by $P_{\mathrm{M}}^{\mathrm{U}}$.

As for the initialization phase of Algorithm I and Algorithm II, the SCA process aimed at solving $(\mathbf{P7})$ is run till the minimum harvested power exceeds P_{Hov} to set the initial UAV locations and the lasers power distribution. Next, the excess remaining power at each UAV over its propulsion power hovering needs is used for transmission with maximum power restriction. Now, this solution is fed to Algorithm II to maximize the minimum rate, and the resulting solution is used as the initial point for Algorithm I.

In the first simulation we study the impact of swarm size on the system performance, with $L = 5$ to give room to multitude of UAVs reach relatively far offshore distances. The total SE and worst-case user performances of the SESCA, and the WSESCA solutions versus the number of UAVs forming the swarm exhibit a unimodal trend with a local maximum, as depicted in Fig. 6 and Fig. 7, respectively. Basically, for small number of UAVs the total emitted power from the laser sources is sufficient to allow them be placed at positions that are closer to the served users and experience favorable channel conditions. In such regime, adding more UAVs will improve the performance as it allows for improving the overall SINR of each user and hence, the achievable SE. Nevertheless, the added UAVs will add more energy expenses to the system, i.e, each UAV need to be supplied with at least the propulsion power needed for hovering. Accordingly, adding more UAVs makes the reachable space for the whole swarm shrinks towards the laser sources centroid. For large number of UAVs the latter effect dominates the gains from having more collaborating transmitters as by then their majority will experience deteriorated channels with users and the overall performance deteriorates. On the other hand, adding UAVs always improves the SEBSCA, WSEBSCA solutions performance as there are no ties for the UAVs to the energy source and they can move freely and occupy favorable positions with respect to the network users. It is worth mentioning that the maximizing number of UAVs heavily depends on the overall available power budget in terms of number of laser sources and their maximum output power as well as their relative positioning with respect to each other and with respect to the served users.

In the second simulation, we vary the laser maximum output power capability and monitor its impact on the considered performance parameters. It is observed in Fig. 8 and Fig. 9 that as $P_{\mathrm{M}}^{\mathrm{L}}$ increases, both the SE and the worst-case user SE increase till a saturation limit. This observation is due to the fact that for the small regime, the harvested power by all the swarm elements barely cater for their hovering propulsion power needs at small distances from the laser sources. As $P_{\mathrm{M}}^{\mathrm{L}}$ increases, the added power budget allows the UAVs to get closer to the users whose majority are located distant from the shore. For extremely large $P_{\mathrm{M}}^{\mathrm{L}}$ values, the problem can be considered unconstrained from a power budget perspective and the solution coincides with the battery powered swarm case. Accordingly, adding more power capability to the laser sources will not impact the preferred UAVs location of service and their transmission powers which already reached its maximum permissible levels. It is important to note that the extreme permissible output optical power values presented in Fig. 8 and Fig. 9 are not meant to be realized in practice by a single laser source but are meant to represent a cluster of laser sources placed close to each other such that the inter-separation distance is negligible compared with the problem spatial scale. In addition, we study the impact of atmospheric turbulence, where in addition to the conducted low atmospheric turbulence simulations, $\alpha_{\mathrm{s}} = 1.59 \times 10^{-4}$, we plot the total and worst-case SE performance of our proposed approaches under moderate turbulence conditions, corresponding to $C_{\mathrm{n}}^{2} = 10^{-14}$ [58], namely, "SESCA Mod. Turb." and "WSESCA Mod. Turb.", respectively. It is observed that, as the atmospheric turbulence becomes more severe, both the total SE and the worst-case SE performances deteriorate, due to less laser energy transmission efficiency which limits the UAVs placement space to a close vicinity surrounding the laser sources, and the problem even becomes infeasible at the lower end of $P_{\mathrm{M}}^{\mathrm{L}}$ values as depicted in Fig. 8 and Fig. 9.

In the third simulation, the lasers centroid x-coordinate is varied to assess the impact of relative placement of lasers with respect to users on the considered performance metrics. As could be seen in Fig. 10 and Fig. 11, both the total SE and worst case SE exhibit a unimodal behavior with a local maximum. This effect is attributed to the fact that lasers locations define the feasible hovering regions for the UAVs. Hence, as the centroid of lasers locations deviates from the centroid of the users' locations, the performance deteriorates due to the UAVs inability to reach points closer to the served users which negatively impacts the channel gains for the communication links between them and the swarm.

In the fourth simulation, we study the potential gains of increasing the UAVs maximum permissible flight altitude on

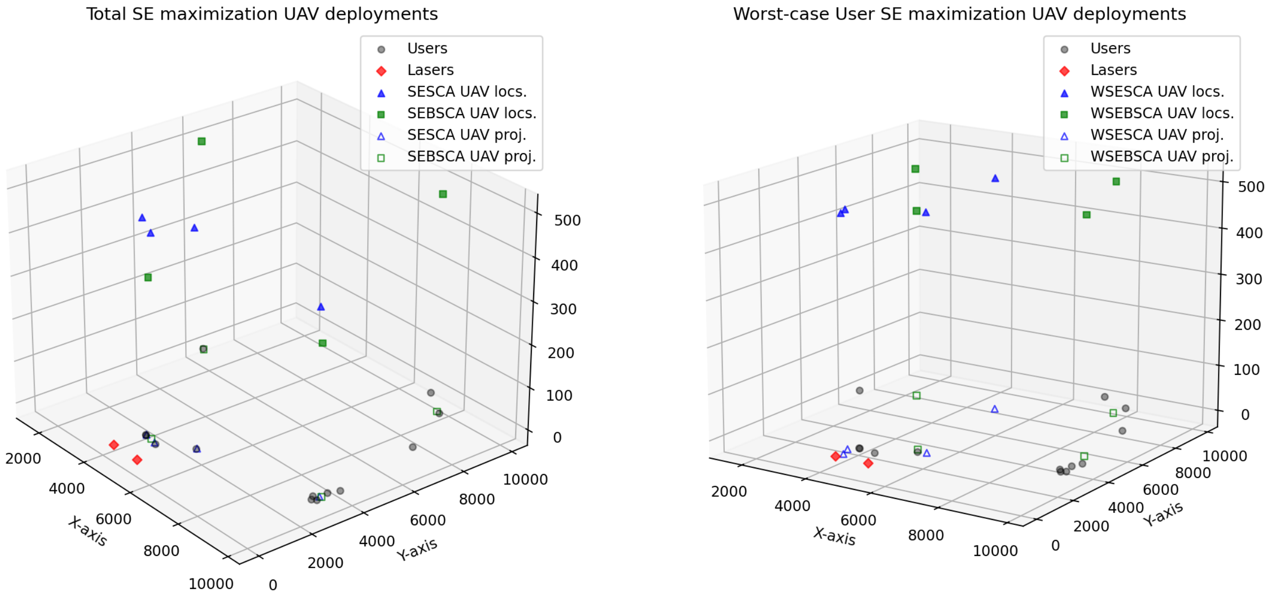
Total SE maximization UAV deployments

Worst-case User SE maximization UAV deployments

FIGURE 5: User layout and placement solutions of the proposed algorithms.

the proposed network performance. It is evident in Fig.12 and Fig. 13 that as the maximum altitude increases the total SE and worst-case SE increase towards a saturation point. For low permissible altitudes, the angles of incidence of laser beams on the UAVs photoelectric converters are large, hence the power harvesting performance deteriorates and limits the UAV range from the laser sources. Similarly, the antenna arrays onboard the UAVs experience larger angles of departure for the majority of radiated beams towards users as the maximum permissible altitude becomes smaller. Consequently, both the SESCA, and the WSESCA solutions push the UAVs to hover at their maximum permissible altitude to relieve the previously mentioned challenges. Nonetheless, increasing the UAVs altitude causes communication links pathloss increase and increased geometric loss for the laser beam reception. Since the gains due to reduced angles of departure and angles of incidence are finite at the high altitude regime the adverse effects of pathloss deterioration and geometric losses dominate. Consequently, the performance saturates at large maximum altitude values as the altitude constraint becomes satisfied with strict inequality.

As for the tethered UAVs optimization solutions, their independence on laser sources parameters is clearly observed in Fig. 10, Fig. 11, Fig. 8, and Fig. 11 as flat curves. As for their dependency on swarm size, it is clearly seen that both the total and minimum spectral efficiency performance exhibit a monotonically increasing behavior that tends to conclude with a saturation behavior as depicted in Fig. 6 and Fig.7, respectively. Such trend owes to the limited space size for UAV placement enforced by the tether length. A similar behavior is observed for the total SE and minimum SE versus the maximum permissible UAV height. Initially, the UAV placement is restricted by the maximum permissible height till it exceeds the tether length. After that increasing the permissible height becomes insignificant, as the UAV motion becomes restricted by the tether length.

Finally, it is observed in Fig. 5, that the worst case SE solutions appearing in the subfigure to the right, tend to keep the UAVs deployed at the maximum height and more attracted to the horizontal centroid to reduce the asymmetry between user channels by increasing distance and angle of departure symmetries. As for the total SE maximization solutions, UAVs tend to get closer to the clustered users and align horizontally with their centroid. Moreover, it is observed that the limited power budget offered to laser powered swarms pushes the UAVs to cluster close to the laser sources while leaving a minority to approach users' locations and experience more favorable channel conditions.

In Fig. 14 and Fig. 15, we plot the objective total spectral efficiency and the worst-case spectral efficiency versus the number of SCA iterations to show the convergence speed of both Algorithm I and Algorithm II, respectively. As observed in both figures the objective value exhibits a non-decreasing trend that reaches saturation for all the considered values for the number of UAVs.

VI. Conclusion

In this paper, we introduced the use of multi-laser powered UAVs featuring hemispherical energy receivers and uniform planar array antennas to provide extended communications coverage for offshore users. We modeled the harvested energy by the hemispherical photoelectric converter and formulated two non-convex optimization problems aimed at the total spectral efficiency maximization and the worst-case user

TABLE 1: User Coordinates and Corresponding Latitudes and Longitudes

User	**1**	**2**	**3**	**4**	**5**	**6**	**7**	**8**	**9**	**10**	**11**	**12**	**13**
X	9625.67	5898.51	1569.17	4520.73	9847.72	4491.17	5047.52	7345.96	9733.35	9734.29	9281.11	9843.00	8344.10
Y	2840.30	1895.74	6160.02	1210.87	3682.31	1227.37	1099.49	9924.17	3299.46	2678.30	7142.16	2781.70	9219.89
Lat.	47.6285	47.5877	47.5232	47.5737	47.6285	47.5733	47.5802	47.5792	47.6284	47.6303	47.6108	47.6313	47.5932
Lon.	-122.3838	-122.3587	-122.3985	-122.3451	-122.3954	-122.3452	-122.3455	-122.4671	-122.3901	-122.3821	-122.4380	-122.3838	-122.4615

TABLE 2: Default Simulation Parameters

D_o	10 cm	$\Delta\theta$	2×10^{-5}	$p_{\mathrm{M}}^{\mathrm{L}}$	5000 W	α_{c}	$10^{-6}\ \mathrm{m}^{-1}$	V_{T}	0.025 V	I_o	10^{-14} A
R_{PD}	1 A/W	r_{PD}	5 cm	$d_{\mathrm{min}}^{\mathrm{c}}$	500 m	$p_{\mathrm{M}}^{\mathrm{U}}$	100 W	α_{s}	1.59×10^{-4}	θ_{err}	2 μrad
γ	2.1	$z_{\mathrm{min}}^{\mathrm{U}}$	40 m	$z_{\mathrm{max}}^{\mathrm{U}}$	500 m	$q_{\mathrm{L}}^{\mathrm{c}}$	5 km	σ^2	-174 dB	f_{c}	8 GHz
$\bar{\alpha}$	100	N_{T}	4	ϵ_{r}	10^{-7}	L	2	U	4	ζ	2

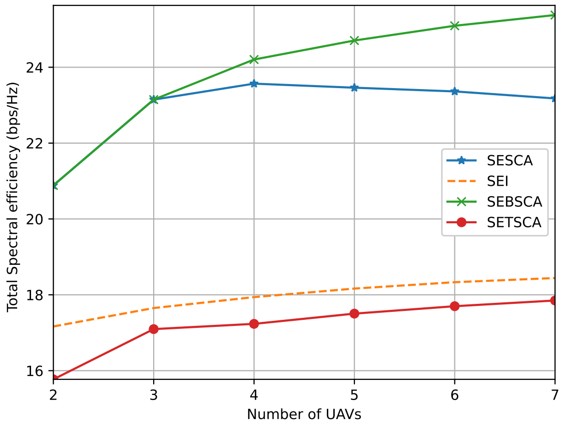

FIGURE 6: Overall SE vs number of UAVs.

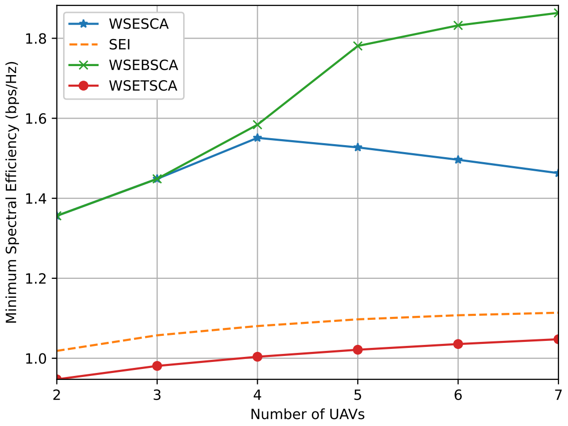

FIGURE 7: Worst-case SE vs number of UAVs.

spectral efficiency maximization. By solving these problems using single-block SCA with novel SCA-compatible bounds for the harvested energy, our simulations demonstrated significant performance gains of 16-33% for total spectral efficiency and 15-40% for worst-case user spectral efficiency, under low turbulence conditions. In addition, it is observed that our proposed multi-laser powered UAV swarm system provides total and worst-case spectral efficiency performance gains, up to 33% and 60%, respectively, compared with the tethered swarm system. As for moderate atmospheric turbulence conditions, the total spectral efficiency performance gain varies between $6 - 13\%$ while the worst-case spectral efficiency performance gain varies between $9 - 15\%$. Our analysis revealed that optimal UAV swarm size generally does not coincide with the affordable maximum, and that the relative positioning of laser sources with respect to the served users critically impacts the system performance. Future research should address mobile maritime users through predictive trajectory optimization, develop distributed control algorithms for larger swarms, and investigate energy-aware scheduling to extend operational range-advancements that would collectively enhance the practical deployment of laser-powered UAV maritime communication systems.

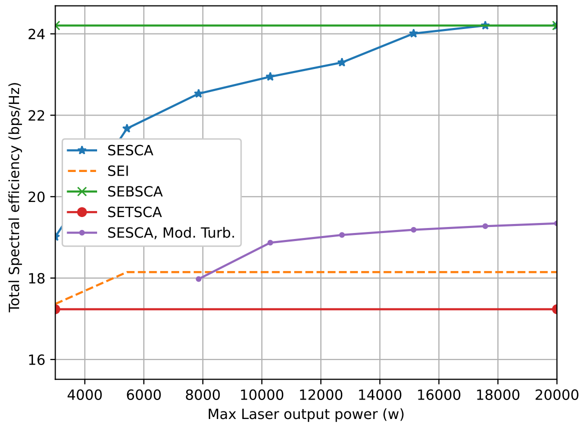

FIGURE 8: Overall SE vs maximum laser power.

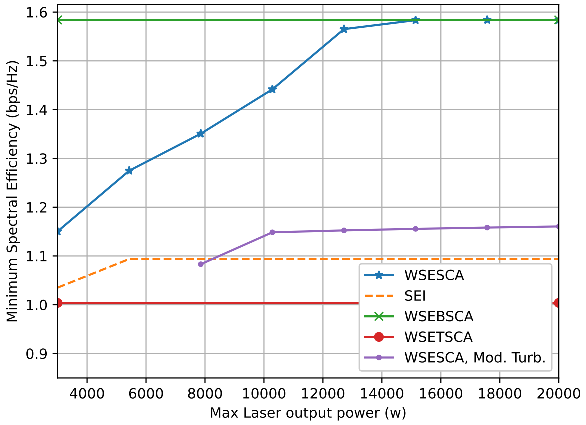

FIGURE 9: Worst-case SE vs maximum laser power.

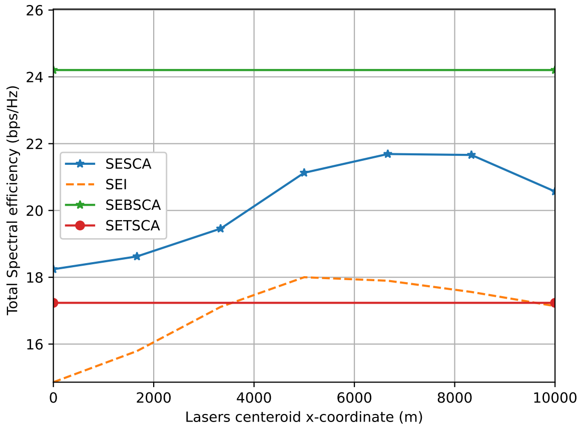

FIGURE 10: Overall SE vs Lasers location.

Appendix A
Derivation of the Harvested Power lower bound

By exploiting the convexity of the function $0.75V_{\rm t}x_i\ln\left(1+x_i/I_o\right)$, the harvested power can be lower bounded using the first-order Taylor series approximation of it as

$$
\begin{aligned}
P_i^{\rm H} &\geq 0.75V_{\rm t}\left(b_{0,i}+b_{1,i}x_i\right), \qquad (15)\\
b_{1,i} &= \frac{x_{i,o}}{I_o+x_{i,o}}+\ln\left(1+\frac{x_{i,o}}{I_o}\right),\\
b_{0,i} &= x_{i,o}\ln\left(1+\frac{x_{i,o}}{I_o}\right)-b_{13}x_{i,o}.
\end{aligned}
$$

The lower bound in (15) does not represent a convex set due to the non-convexity of x w.r.t the optimization variables. Since $b_{1,i}\geq 0$, we lower bound x_i by exploiting the convexity of $P_{i,\ell}^{\rm d}$ in $d_{i,\ell}$ using its first-order Taylor series

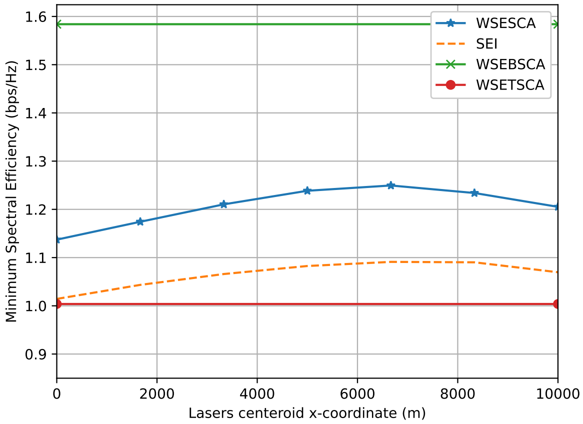

FIGURE 11: Worst-case SE vs Lasers location.

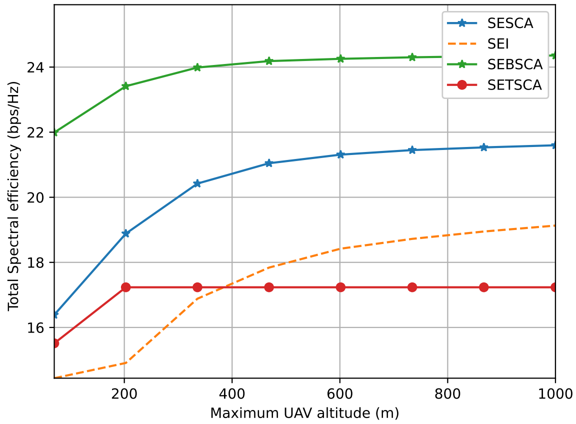

FIGURE 12: Overall SE vs UAV maximum height.

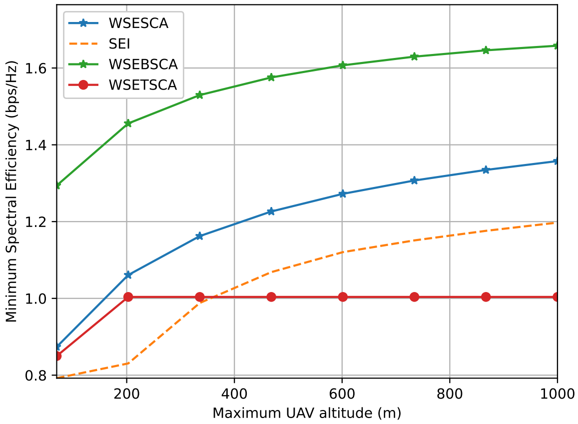

FIGURE 13: Worst-case SE vs UAV maximum height.

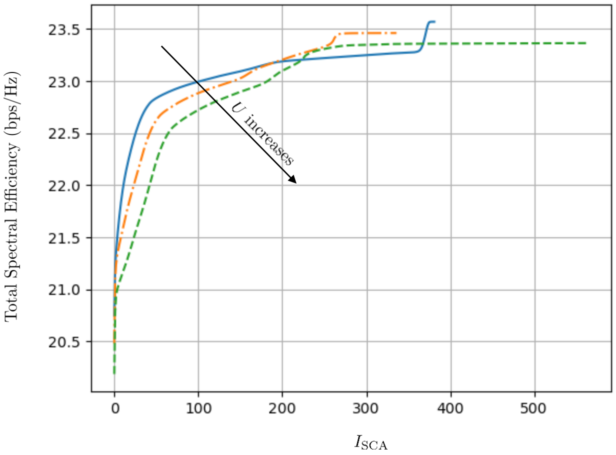

FIGURE 14: Convergence behavior of Algorithm I for $U \in \{4, 5, 6\}$.

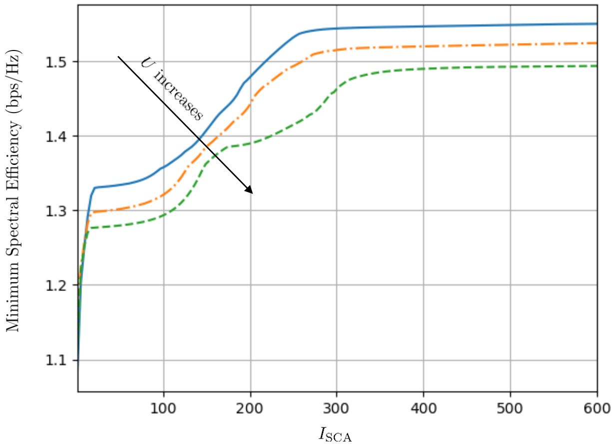

FIGURE 15: Convergence behavior of Algorithm II for $U \in \{4, 5, 6\}$.

approximation as

$$x_i \geq x_i^{\mathrm{LB}} = R_{\mathrm{pd}} e^{-\frac{\theta_{\mathrm{err}}}{\Delta\theta}} \frac{\pi r_{\mathrm{pd}}^2}{2} \sum_{\ell=1}^{L} \left(1 + \frac{q_{i,\mathrm{z}}^{\mathrm{u}} - q_{\ell,\mathrm{z}}^{\mathrm{L}}}{d_{i,\ell}^{\mathrm{L}}}\right) \times P_{i,\ell}^{\mathrm{L}} \left(b_{2,i,\ell} + b_{3,i,\ell} d_{i,\ell}^{\mathrm{L}}\right) \qquad (16)$$

$$b_{3,i,\ell} = -\frac{e^{-\alpha d_{i,\ell,o}^{\mathrm{L}}} \left(\alpha D_{\mathrm{o}} + \Delta\theta(\alpha d_{i,\ell,o}^{\mathrm{L}} + 2)\right)}{{r_{i,\ell,o}^{\mathrm{L}}}^{3}},$$

$$b_{2,i,\ell} = \frac{e^{-\alpha d_{i,\ell,o}^{\mathrm{L}}}}{r_{i,\mathrm{L},\mathrm{o}}^2} - b_{3,i,\ell} d_{i,\ell,o}^{\mathrm{L}}, \quad r_{i,\mathrm{L},\mathrm{o}} = D_o + \Delta\theta d_{i,\ell,o}.$$

The previous bound is still not a concave bound, due to the non-convexity of the effective area terms and the products involving the laser output power and the distance terms. Hence, we first re-arrange x_i^{LB} as

$$x_i^{\mathrm{LB}} = R_{\mathrm{pd}} e^{-\frac{\theta_{\mathrm{err}}}{\Delta\theta}} \frac{\pi r_{\mathrm{pd}}^2}{2} \left(\sum_{\ell=1}^{L} P_{i,\ell}^{\mathrm{L}} \left(b_{2,i,\ell} + b_{3,i,\ell} d_{i,\ell}^{\mathrm{L}}\right) + b_{2,i,\ell} \frac{q_{i,\mathrm{z}}^{\mathrm{u}} - q_{\ell,\mathrm{z}}^{\mathrm{L}}}{d_{i,\ell}^{\mathrm{L}}} P_{i,\ell}^{\mathrm{L}} + b_{3,i,\ell} \left(q_{i,\mathrm{z}}^{\mathrm{u}} - q_{\ell,\mathrm{z}}^{\mathrm{L}}\right) P_{i,\ell}^{\mathrm{L}} \right). \qquad (17)$$

By examining the previous equation, it is vivid that except for the function $\frac{1}{d_{i,\ell}^{\mathrm{L}}}$, the bound consists of additions and subtractions of products of positive convex functions. In order to exploit the bounds in Appendix B, we use the following difference of convex (DC) decomposition for $\frac{1}{d_{i,\ell}^{\mathrm{L}}}$,

$$\frac{1}{d_{i,\ell}^{\mathrm{L}}} = \frac{1}{d_{i,\ell}^{\mathrm{L}}} + \frac{d_{i,\ell}^{\mathrm{L}}}{d_{\mathrm{min,L}}^2} - \frac{d_{i,\ell}^{\mathrm{L}}}{d_{\mathrm{min,L}}^2}, \qquad (18)$$

where $d_{\mathrm{min,L}}$ is a lower bound on the distance between any UAV and any laser source guaranteed by permissible flight ranges and restrictions on laser locations. By substituting (18) in (17), and re-arranging terms, we get

$$x_i^{\mathrm{LB}} = R_{\mathrm{pd}} e^{-\frac{\theta_{\mathrm{err}}}{\Delta\theta}} \frac{\pi r_{\mathrm{pd}}^2}{2} \sum_{\ell=1}^{L} b_{2,i,\ell} P_{i,\ell}^{\mathrm{L}} + b_{3,i,\ell} \underbrace{P_{i,\ell}^{\mathrm{L}} d_{i,\ell}^{\mathrm{L}}}_{T_1} + \frac{b_{3,i,\ell}}{4} \left(q_{i,\mathrm{z}}^{\mathrm{u}} - q_{\ell,\mathrm{z}}^{\mathrm{L}} + P_{i,\ell}^{\mathrm{L}}\right)^2 - \underbrace{\frac{b_{3,i,\ell}}{4} \left(q_{i,\mathrm{z}}^{\mathrm{u}} - q_{\ell,\mathrm{z}}^{\mathrm{L}} - P_{i,\ell}^{\mathrm{L}}\right)^2}_{T_2} + \frac{b_{2,i,\ell}}{4} \Bigg(\underbrace{\left(q_{i,\mathrm{z}}^{\mathrm{u}} - q_{\ell,\mathrm{z}}^{\mathrm{L}} + P_{i,\ell}^{\mathrm{L}}\right)^2 \left(\frac{1}{d_{i,\ell}^{\mathrm{L}}} + \frac{d_{i,\ell}^{\mathrm{L}}}{d_{\mathrm{min,L}}^2}\right)}_{T_3} + \underbrace{\left(q_{i,\mathrm{z}}^{\mathrm{u}} - q_{\ell,\mathrm{z}}^{\mathrm{L}} - P_{i,\ell}^{\mathrm{L}}\right)^2 \frac{d_{i,\ell}^{\mathrm{L}}}{d_{\mathrm{min,L}}^2}}_{T_4} - \underbrace{\left(q_{i,\mathrm{z}}^{\mathrm{u}} - q_{\ell,\mathrm{z}}^{\mathrm{L}} + P_{i,\ell}^{\mathrm{L}}\right)^2 \frac{d_{i,\ell}^{\mathrm{L}}}{d_{\mathrm{min,L}}^2}}_{T_5} \underbrace{- \left(q_{i,\mathrm{z}}^{\mathrm{u}} - q_{\ell,\mathrm{z}}^{\mathrm{L}} - P_{i,\ell}^{\mathrm{L}}\right)^2 \left(\frac{1}{d_{i,\ell}^{\mathrm{L}}} + \frac{d_{i,\ell}^{\mathrm{L}}}{d_{\mathrm{min,L}}^2}\right)}_{T_6} \Bigg). \qquad (19)$$

Now, the non-convex terms in (19) are $T_1 \ldots T_6$, so we derive an SCA-compatible concave lower bound to x_i^{LB} by leftmargin=10pt

- upper bounding T_1 using theorem 1 in Appendix B, (Note that $b_{3,i,\ell} \leq 0 \; \forall i, \ell$),
- upper bounding T_2 using its first-order Taylor series approximation due its concavity,
- lower bounding T_3 and T_4 using theorem 2 in Appendix B
- upper bounding T_5 and T_6 using theorem 1 in Appendix B.

Consequently, we get $\tilde{x}_i^{\mathrm{LB}} \leq x_i^{\mathrm{LB}}$, expressed as

$$\begin{aligned}
\tilde{x}_i^{\mathrm{LB}} &= R_{\mathrm{pd}} e^{-\frac{\theta_{\mathrm{err}}}{\Delta\theta}} \frac{\pi r_{\mathrm{pd}}^2}{2} \sum_{\ell=1}^{L} b_{2,i,\ell} P_{i,\ell}^{\mathrm{L}} + b_{3,i,\ell} F_{\mathrm{UB}}^{\mathrm{Cvx}} \left[P_{i,\ell}^{\mathrm{L}}, d_{i,\ell}^{\mathrm{L}}\right] \\
&+ \frac{b_{3,i,\ell}}{4} \left(\left(q_{i,\mathrm{z}}^{\mathrm{u}} - q_{\ell,\mathrm{z}}^{\mathrm{L}} + P_{i,\ell}^{\mathrm{L}}\right)^2 - \mathrm{F.o.T} \left[\left(q_{i,\mathrm{z}}^{\mathrm{u}} - q_{\ell,\mathrm{z}}^{\mathrm{L}} - P_{i,\ell}^{\mathrm{L}}\right)^2 \right] \right) \\
&+ \frac{b_{2,i,\ell}}{4} \Bigg(F_{\mathrm{LB}}^{\mathrm{Cvx}} \left[\left(q_{i,\mathrm{z}}^{\mathrm{u}} - q_{\ell,\mathrm{z}}^{\mathrm{L}} + P_{i,\ell}^{\mathrm{L}}\right)^2, \frac{1}{d_{i,\ell}^{\mathrm{L}}} + \frac{d_{i,\ell}^{\mathrm{L}}}{d_{\mathrm{min,L}}^2} \right] \\
&+ F_{\mathrm{LB}}^{\mathrm{Cvx}} \left[\left(q_{i,\mathrm{z}}^{\mathrm{u}} - q_{\ell,\mathrm{z}}^{\mathrm{L}} - P_{i,\ell}^{\mathrm{L}}\right)^2, \frac{d_{i,\ell}^{\mathrm{L}}}{d_{\mathrm{min,L}}^2} \right] \\
&- F_{\mathrm{UB}}^{\mathrm{Cvx}} \left[\left(q_{i,\mathrm{z}}^{\mathrm{u}} - q_{\ell,\mathrm{z}}^{\mathrm{L}} + P_{i,\ell}^{\mathrm{L}}\right)^2, \frac{d_{i,\ell}^{\mathrm{L}}}{d_{\mathrm{min,L}}^2} \right] \\
&- F_{\mathrm{UB}}^{\mathrm{Cvx}} \left[\left(q_{i,\mathrm{z}}^{\mathrm{u}} - q_{\ell,\mathrm{z}}^{\mathrm{L}} - P_{i,\ell}^{\mathrm{L}}\right)^2, \frac{1}{d_{i,\ell}^{\mathrm{L}}} + \frac{d_{i,\ell}^{\mathrm{L}}}{d_{\mathrm{min,L}}^2} \right] \Bigg). \qquad (20)
\end{aligned}$$

Finally, the harvested power lower bound is reached by replacing x_i in (15) with $\tilde{x}_i^{\mathrm{LB}}$, and is expressed as

$$\tilde{P}_i^{\mathrm{H}} = 0.75 V_{\mathrm{t}} \left(b_{0,i} + b_{1,i} \tilde{x}_i^{\mathrm{LB}}\right). \qquad (21)$$

Appendix B
Theorems for SCA-compatible bounds

Theorem 1. *If* $f(\boldsymbol{x}) \geq 0,\ \forall \boldsymbol{x} \in \mathcal{D}_1$, *and* $g(\boldsymbol{y}) \geq 0,\ \forall \boldsymbol{y} \in \mathcal{D}_2$, $f(.), g(.)$ *are both convex over* $\mathcal{D}_1$, $\mathcal{D}_2$, *respectively, then [42, Th. 1]*

$$\begin{aligned}
f(\boldsymbol{x}) g(\boldsymbol{y}) \leq F_{\mathrm{UB}}^{\mathrm{Conv}}[f, g] = \frac{1}{4}\big(f_{\mathrm{s}}^2 + f_{\mathrm{d},o}^2 - 2 f_{\mathrm{d},o} \\
\times \big(I_1\big(\tilde{f}_{\mathrm{s}} - f_{\mathrm{s}}\big) + f(\boldsymbol{x}) - \tilde{g}(\boldsymbol{y})\big)\big), \forall (\boldsymbol{x}, \boldsymbol{y}) \in \hat{\mathcal{D}},
\end{aligned}$$

s.t. $f_{\mathrm{s}} = f(\boldsymbol{x}) + g(\boldsymbol{y})$, $f_{\mathrm{d},o} = f(\boldsymbol{x}_o) - g(\boldsymbol{y}_o)$, $I_1 = 1$ *if* $f_{\mathrm{d},0} \geq 0$, $I_1 = 0$ *o.w.*, $\tilde{\chi}(\boldsymbol{z}) = \chi(\boldsymbol{z}_o) + \nabla \chi^{\mathrm{T}}(\boldsymbol{z}_o)(\boldsymbol{z} - \boldsymbol{z}_o)$, $\hat{\mathcal{D}} = \mathcal{D}_1 \times \mathcal{D}_2$.

Theorem 2. *If* $f(\boldsymbol{x}) \geq 0,\ \forall \boldsymbol{x} \in \mathcal{D}_1$, *and* $g(\boldsymbol{y}) \geq 0,\ \forall \boldsymbol{y} \in \mathcal{D}_2$, $f(.), g(.)$ *are both convex over* $\mathcal{D}_1$, $\mathcal{D}_2$, *respectively, then [59, Th. 2]*

$$\begin{aligned}
f(\boldsymbol{x}) g(\boldsymbol{y}) \geq F_{\mathrm{LB}}^{\mathrm{Conv}}(\boldsymbol{x}, \boldsymbol{y}) = \frac{\left(f(\boldsymbol{x_o}) + g(\boldsymbol{y_o})\right)^2}{2} + (f(\boldsymbol{x_o}) \\
+ g(\boldsymbol{y_o}))\Big(\nabla f^{\mathrm{T}}(\boldsymbol{x_o})\,(\boldsymbol{x} - \boldsymbol{x_o}) + \nabla g^{\mathrm{T}}(\boldsymbol{y_o})\,(\boldsymbol{y} - \boldsymbol{y_o})\Big) \\
- \frac{f^2(\boldsymbol{x})}{2} - \frac{g^2(\boldsymbol{y})}{2} \quad \forall (\boldsymbol{x}, \boldsymbol{y}) \in \mathcal{D}_1 \times \mathcal{D}_2, (\boldsymbol{x_o}, \boldsymbol{y_o}) \in \mathcal{D}_1 \times \mathcal{D}_2.
\end{aligned}$$

REFERENCES

[1] ShipHire, “Growth of the maritime industry over the past decade,” https://www.marinohire.com/blog/growth-of-the-maritime-industry-over-the-past-decade, accessed: 2025-4-24.

[2] F. S. Alqurashi, A. Trichili, N. Saeed, B. S. Ooi, and M.-S. Alouini, “Maritime communications: A survey on enabling technologies, opportunities, and challenges,” *IEEE Internet Things J.*, vol. 10, 2022.

[3] R. Campos, T. Oliveira, N. A. Cruz, A. Matos, and J. M. Almeida, “BLUECOM+: Cost-effective broadband communications at remote ocean areas,” *OCEANS 2016 - Shanghai*, 2016.

[4] S. Sinha, S. Y. Kwon, and S.-H. Park, “A survey of deep/machine learning in maritime communications,” *2023 Fourteenth Int. Conf. on Ubiquit. and Future Netw. (ICUFN)*.

[5] A. A. Khuwaja, Y. Chen, N. Zhao, M.-S. Alouini, and P. Dobbins, “A survey of channel modeling for UAV communications,” *IEEE Commun. Surveys Tuts.*, vol. 20, 2018.

[6] E. Impact, “Global maritime trends 2050,” https://impact.economist.com/ocean/global-maritime-trends-2050/, Nov. 2023, accessed: 2025-4-24.

[7] Z.-X. Zhou, N. Ge, and Z. Wang, “Two-timescale beam selection and power allocation for maritime offshore communications,” *IEEE Trans. Wireless Commun.*, vol. 25, 2021.

[8] R. Duan, J. Wang, H. Zhang, Y. Ren, and L. Hanzo, “Joint multicast beamforming and relay design for maritime communication systems,” *IEEE Trans. Green Commun. Netw.*, vol. 4, 2020.

[9] X. Cao, X. Hu, and M. Peng, “Joint mode selection and beamforming for IRS-aided maritime cooperative communication systems,” *IEEE Trans. Green Commun. Netw.*, vol. 7, 2023.

[10] K. Li, M. Cui, G. Zhang, Q. Wu, D. Li, and J. He, “Robust transmit and reflect beamforming design for IRS-assisted offshore NOMA communication systems,” *IEEE Trans. Veh. Technol.*, vol. 73, 2024.

[11] S. Ammar, C. Pong Lau, and B. Shihada, “An in-depth survey on virtualization technologies in 6G integrated terrestrial and non-terrestrial networks,” *IEEE Open J. Commun. Soc.*, vol. 5, pp. 3690–3734, 2024.

[12] W. Abderrahim, O. Amin, M.-S. Alouini, and B. Shihada, “Proactive traffic offloading in dynamic integrated multisatellite terrestrial networks,” *IEEE Trans. Commun.*, vol. 70, no. 7, pp. 4671–4686, 2022.

[13] B. Shang, “Fundamentals of satellite-maritime communications: Downlink and uplink analysis,” *IEEE Trans. Commun.*, 2024.

[14] K. Xiong, X. Chen, and M. Ying, “Robust beamforming design for integrated satellite-terrestrial maritime communications in the presence of wave fluctuation,” *IEEE Internet Things J.*, vol. 11, 2024.

[15] X. Fang, W. Feng, Y. Wang, Y. Chen, N. Ge, Z. Ding, and H. Zhu, “NOMA-based hybrid satellite-UAV-terrestrial networks for 6G maritime coverage,” *IEEE Trans. Wireless Commun.*, vol. 22, 2021.

[16] Y. Wang, X. Fang, W. Feng, Y. Chen, N. Ge, and Z. Lu, “On-demand coverage for maritime hybrid satellite-UAV-terrestrial networks,” *2020 Int. Conf. on Wirel. Commun. and Signal Process. (WCSP)*, 2020.

[17] N. Nomikos, P. K. Gkonis, P. S. Bithas, and P. Trakadas, “A survey on UAV-aided maritime communications: Deployment considerations, applications, and future challenges,” *IEEE Open J. Commun. Soc.*, vol. 4, 2022.

[18] A. T. Çagan, G. B. Koç, H. Yakin, B. Çiloglu, M. Z. Asghar, Ö. Ersoy, J. Hämäläinen, and M. Öztürk, “UAV-based maritime communications: Relaying to enhance the link quality,” *ArXiv*, 2023.

[19] K. Lin, H. Yang, M. Zheng, L. Xiao, C. Huang, and D. T. Niyato, “Penalized reinforcement learning-based energy-efficient UAV-RIS assisted maritime uplink communications against jamming,” *IEEE Trans. Veh. Technol.*, vol. 73, 2024.

[20] H. Zhang and L. H. Hanzo, “Aerial reconfigurable intelligent surface assisted maritime wireless communications,” *2022 14th Int. Conf. on Wirel. Commun. & Signal Process. (WCSP)*, 2022.

[21] H. Yang, K. Lin, L. Xiao, Y. Zhao, Z. Xiong, and Z. Han, “Energy harvesting UAV-RIS-assisted maritime communications based on deep reinforcement learning against jamming,” *IEEE Trans. Wireless Commun.*, vol. 23, 2024.

[22] H. El Hammouti, M. Benjillali, B. Shihada, and M.-S. Alouini, “Learn-as-you-fly: A distributed algorithm for joint 3D placement and user association in multi-UAVs networks,” *IEEE Trans. Wireless Comm.*, vol. 18, no. 12, pp. 5831–5844, 2019.

[23] H. El Hammouti, D. Hamza, B. Shihada, M.-S. Alouini, and J. S. Shamma, “The optimal and the greedy: Drone association and positioning schemes for internet of uavs,” *IEEE Internet Things J.*, vol. 8, no. 18, pp. 14 066–14 079, 2021.

[24] M. M. Azari, Y. Murillo, O. Amin, F. Rosas, M.-S. Alouini, and S. Pollin, “Coverage maximization for a poisson field of drone cells,” in *2017 IEEE 28th Annual Int. Symp. on Pers., Indoor, & Mobil. Radio Commun. (PIMRC)*. IEEE, 2017, pp. 1–6.

[25] J. Liu, F. Zeng, W. Wang, Z. Sheng, X. Wei, and K. Cumanan, “Trajectory design for UAV-enabled maritime secure communications: A reinforcement learning approach,” *China Communications*, vol. 19, 2022.

[26] Z. Zhang, T. Peng, K. Yang, and X. Li, “Trajectory optimization and retrieving monitory system for UAV-assisted offshore maritime communications,” *2023 3rd Int. Conf. on Electron. Inf. Eng. & Comput. Sci. (EIECS)*, 2023.

[27] L. Zhang, A. Celik, S. Dang, and B. Shihada, “Energy-efficient trajectory optimization for UAV-assisted IoT networks,” *IEEE Trans. Mobile Comput.*, vol. 21, no. 12, pp. 4323–4337, 2021.

[28] H. Li, C. Yu, C. Zhang, H. Jiao, B. Lin, and R. He, “Maritime multi-relay communications based on UAV trajectory adjustment and dual q-learning,” *2021 Int. Conf. on Secur., Pattern Anal., Cybern. (SPAC)*, 2021.

[29] L. Liu, B. Lin, and Y. Che, “Joint UAV-BS deployment and power allocation for maritime emergency communication system,” in *2021 13th Int. Conf. on Wirel. Commun. & Signal Process. (WCSP)*. IEEE, 2021, pp. 1–5.

[30] S. Ammar, O. Amin, and B. Shihada, “Tethered UAV-based communications for under-connected near-shore maritime areas,” *2024 IEEE Int. Black Sea Conf. Commun. and Netw. (BlackSeaCom)*, 2024.

[31] K. Singh, P. S. Raut, P. K. Sharma, and C.-P. Li, “Laser-powered multi-UAV URLLC systems: Reliability and scheduling performance analysis,” *IEEE Trans. on Veh. Technol.*, vol. 72, 2023.

[32] X. Ma, X. Liu, and N. Ansari, “Green laser-powered UAV far-field wireless charging and data backhauling for a large-scale sensor network,” *IEEE Internet Things J.*, 2024.

[33] D. Li, S. Xu, C. Zhao, Y. Wang, R. Xu, and B. Ai, “Data collection in laser-powered UAV-assisted IoT networks: Phased scheme design based on improved clustering algorithm,” *IEEE Trans. Green Commun. Netw.*, vol. 8, pp. 482–497, 2024.

[34] W. Liu, L. Zhang, and N. Ansari, “Laser charging enabled DBS placement for downlink communications,” *IEEE Trans. Netw. Sci. Eng.*, vol. 8, no. 4, pp. 3009–3018, 2021.

[35] J. Ouyang, Y. Che, J. Xu, and K. Wu, “Throughput maximization for laser-powered UAV wireless communication systems,” in *2018 IEEE Int. Conf. Commun. Workshops (ICC Workshops)*. IEEE, 2018, pp. 1–6.

[36] Z. Cheng, Z. Gao, M. Liwang, L. Huang, X. Du, and M. Guizani, “Intelligent task offloading and energy allocation in the UAV-aided mobile edge-cloud continuum,” *IEEE Network*, vol. 35, no. 5, pp. 42–49, 2021.

[37] W. Jaafar and H. Yanikomeroglu, “Dynamics of laser-charged UAVs: A battery perspective,” *IEEE Internet Things J.*, vol. 8, no. 13, pp. 10 573–10 582, 2020.

[38] M.-M. Zhao, Q. Shi, and M.-J. Zhao, “Efficiency maximization for UAV-enabled mobile relaying systems with laser charging,” *IEEE Trans. Wireless Commun.*, vol. 19, no. 5, pp. 3257–3272, 2020.

[39] A. Ranjha and G. Kaddoum, “URLLC-enabled by laser powered UAV relay: A quasi-optimal design of resource allocation, trajectory planning and energy harvesting,” *IEEE Trans. Veh. Technol.*, 2021.

[40] X. Zhao, Y. Zhong, Z. Mao, and X. He, “Performance optimization of multilink laser powered UAV relay systems,” *Scientific Reports*, vol. 15, no. 1, p. 12701, 2025.

[41] A. M. Abdelhady, A. Çelik, C. Diaz-Vilor, H. Jafarkhani, and A. M. Eltawil, “Operation optimization of laser-powered aerial data harvesting for passive IoT networks,” in *IEEE Wireless Commun. and Netw. Conf. (WCNC)*. IEEE, 2024, pp. 1–6.

[42] A. M. Abdelhady, A. Celik, C. Diaz-Vilor, H. Jafarkhani, and A. M. Eltawil, “Laser-empowered UAVs for aerial data aggregation in passive IoT networks,” *IEEE Open J. Commun. Soc.*, 2024.

[43] S. Jayaprakasam, S. K. A. Rahim, and C. Y. Leow, “Distributed and collaborative beamforming in wireless sensor networks: Classifications, trends, and research directions,” *IEEE Commun. Surveys Tuts.*, vol. 19, no. 4, pp. 2092–2116, 2017.

[44] Y. S. Meng and Y. H. Lee, “Measurements and characterizations of air-to-ground channel over sea surface at c-band with low airborne altitudes,” *IEEE Trans. Veh. Technol.*, vol. 60, no. 4, pp. 1943–1948, 2011.

[45] J. Wang, H. Zhou, Y. Li, Q. Sun, Y. Wu, S. Jin, T. Q. Quek, and C. Xu, “Wireless channel models for maritime communications,” *IEEE Access*, vol. 6, pp. 68 070–68 088, 2018.

[46] L. Yee Hui, F. Dong, and Y. S. Meng, “Near sea-surface mobile radiowave propagation at 5 GHz: measurements and modeling,” *Radioengineering*, vol. 23, no. 3, pp. 824–830, 2014.

[47] C. A. Balanis, *Antenna Theory: Analysis and Design*, 4th ed. Wiley, 2016.

[48] E. Lorenzo, *Solar electricity: engineering of photovoltaic systems*. Earthscan/James & James, 1994.

[49] H. Kaushal, V. Jain, and S. Kar, *Free space optical communication*. Springer, 2017.

[50] Y. Kaymak, R. Rojas-Cessa, J. Feng, N. Ansari, M. Zhou, and T. Zhang, “A survey on acquisition, tracking, and pointing mechanisms for mobile free-space optical communications,” *IEEE Commun. Surveys Tuts.*, vol. 20, no. 2, pp. 1104–1123, 2018.

[51] C. E. Shannon, “A mathematical theory of communication,” *The Bell system technical journal*, vol. 27, no. 3, pp. 379–423, 1948.

[52] Y. Zeng, J. Xu, and R. Zhang, “Energy minimization for wireless communication with rotary-wing UAV,” *IEEE Trans. Wireless Commun.*, vol. 18, no. 4, pp. 2329–2345, 2019.

[53] M. Razaviyayn, “Successive convex approximation: Analysis and applications,” Ph.D. dissertation, University of Minnesota, 2014.

[54] N. O. for Coastal Management, “Ais data for 2024,” https://coast.noaa.gov/htdata/CMSP/AISDataHandler/2024/index.html, [Online]. Available: https://coast.noaa.gov/htdata/CMSP/AISDataHandler/2024/index.html. [Accessed 16 Apr. 2025].

[55] J. D. Griffin and G. D. Durgin, “Complete link budgets for backscatter-radio and RFID systems,” *IEEE Antennas Propag. Mag.*, vol. 51, no. 2, pp. 11–25, 2009.

[56] Y. Sun, D. Xu, D. W. K. Ng, L. Dai, and R. Schober, “Optimal 3D-trajectory design and resource allocation for solar-powered UAV communication systems,” *IEEE Trans. Commun.*, vol. 67, no. 6, 2019.

[57] “Safe-t2 advanced tethered drone station,” https://elistair.com/solutions/tethering-station-safe-t/, accessed: 2026-03-29.

[58] S. S. Muhammad, P. Kohldorfer, and E. Leitgeb, “Channel modeling for terrestrial free space optical links,” in *Proceedings of 2005 7th International Conference Transparent Optical Networks, 2005.*, vol. 1. IEEE, 2005, pp. 407–410.

[59] A. M. Abdelhady, C. Diaz-Vilor, M. Barzegaran, H. Jafarkhani, and A. M. Eltawil, “Optimization of hybrid Laser-Battery-Powered UAV-Assisted backscatter communications,” *IEEE Trans. Commun.*, 2025.